Editors' Suggestion

Effect of shock waves on the statistics and scaling in compressible isotropic turbulence

Jianchun Wang,[1,*] Minping Wan,[1,†] Song Chen,[1] Chenyue Xie,[1] and Shiyi Chen[1,2]

[1]*Department of Mechanics and Aerospace Engineering, Southern University of Science and Technology, Shenzhen, Guangdong 518055, People's Republic of China*

[2]*State Key Laboratory of Turbulence and Complex Systems, Center for Applied Physics and Technology, College of Engineering, Peking University, Beijing 100871, People's Republic of China*

(Received 3 January 2018; published 11 April 2018)

The statistics and scaling of compressible isotropic turbulence in the presence of large-scale shock waves are investigated by using numerical simulations at turbulent Mach number M_t ranging from 0.30 to 0.65. The spectra of the compressible velocity component, density, pressure, and temperature exhibit a k^{-2} scaling at different turbulent Mach numbers. The scaling exponents for structure functions of the compressible velocity component and thermodynamic variables are close to 1 at high orders $n \geqslant 3$. The probability density functions of increments of the compressible velocity component and thermodynamic variables exhibit a power-law region with the exponent -2. Models for the conditional average of increments of the compressible velocity component and thermodynamic variables are developed based on the ideal shock relations and are verified by numerical simulations. The overall statistics of the compressible velocity component and thermodynamic variables are similar to one another at different turbulent Mach numbers. It is shown that the effect of shock waves on the compressible velocity spectrum and kinetic energy transfer is different from that of acoustic waves.

DOI: 10.1103/PhysRevE.97.043108

I. INTRODUCTION

Compressible turbulence plays an important role in many natural phenomena and industrial applications, including interstellar turbulence, inertial confinement fusion, and the designs of supersonic aircrafts and scramjets. Statistics and structures of compressible turbulence are more complex than those of incompressible turbulence, due to the strong couplings between the velocity field and thermodynamic fields [1–12]. In addition to vortex structures, there are shock waves generated from compressible turbulence. The scaling and intermittency of compressible turbulence can be different from those of incompressible turbulence, due to the interaction between vortex structures and shock waves.

According to the traditional Richardson-Kolmogorov-Onsager picture, kinetic energy cascades conservatively from large scales to small scales in an inertial range of three-dimensional fully developed incompressible turbulence at very high Reynolds number [13]. Due to the pressure-dilatation correlation, kinetic energy is not an ideal invariant of compressible Navier-Stokes equations. Thus, the notion of kinetic energy cascade in compressible turbulence is not as clear as that in incompressible turbulence. Aluie's pioneer work [14,15] demonstrated the existence of an inertial range over which kinetic energy cascades locally and in a conservative fashion in compressible turbulence, provided that the pressure-dilatation cospectrum decays at a sufficiently rapid rate. The analysis was based on the Favre filtering approach and was further verified by numerical simulations of both forced and decaying compressible isotropic turbulence [16]. Moreover, Kolmogorov's 4/5 law for energy flux is an exact result in incompressible turbulence, which provides a strong foundation for the constant energy flux in the inertial range [13]. Similar relations in compressible turbulence have been studied recently. Falkovich *et al.* derived an exact physical-space flux relation for compressible turbulence analogous to the Kolmogorov flux relation for incompressible turbulence [17]. Wagner *et al.* further studied and modified the flux relation by numerical simulation of three-dimensional supersonic isothermal turbulence [18]. Galtier and Banerjee [19] derived an exact fourth-order relation for correlation functions in compressible isothermal turbulence, which was verified numerically by Kritsuk *et al.* in three-dimensional supersonic isothermal turbulence [20]. Wang *et al.* [21] examined the kinetic energy cascade by Fourier analysis, a new exact physical-space flux relation and the Favre filtering approach in a numerically simulated compressible turbulence. Eyink and Drivas [22] made a profound theoretical analysis on the dissipative anomalies of both kinetic energy and entropy in compressible turbulence. Their analysis indicated that the singularity of shock structure is important for cascades of both kinetic energy and entropy in the limit of high Reynolds number and Peclet number in compressible turbulence.

As a nonlinear model of three-dimensional hydrodynamic turbulence, Burgers turbulence has been frequently investigated by both theoretical analysis and numerical simulations since the pioneering work done by Burgers [23]. A number of studies have demonstrated the significant impact of shock waves on the statistical properties of Burgers turbulence [24–32]. For the stationary Burgers turbulence driven by large-scale force, isolated shocks connected by smooth ramps could be identified, leading to the bifractal scaling exponents of the

*wangjc@sustc.edu.cn
†wanmp@sustc.edu.cn

velocity structure function: the scaling exponent equals to n at orders $n \leqslant 1$ and equals to 1 at orders $n \geqslant 1$ [13,24,33]. For the stationary Burgers turbulence driven by a multiscaling force, the multiscaling behaviors of the velocity structure function were found: the scaling exponent of the velocity structure function asymptotically saturates to 1 with increasing orders [25]. The probability density function (PDF) of the velocity derivative in Burgers turbulence has attracted many attentions [26–31]. It was found that due to the large negative velocity gradients stem from preshocks, the left tail of the PDF of the velocity derivative exhibits the $-7/2$ power-law scaling [29–32].

Shock waves in three-dimensional compressible flows are more complicated than those in Burgers turbulence. Velocity jumps across shock waves of compressible flows are coupled with thermodynamic properties through ideal shock relations. To isolate the effect of shock waves on turbulence, lots of efforts have been devoted to the problem of the isotropic turbulence interacting with a single shock wave [34–41]. The traditional numerical approach to the problem of shock-turbulence interaction is very expensive even when a shock capturing scheme is used [41]. Most studies are limited to the low Reynolds numbers. Recently, Ryu and Livescu showed that the shock-turbulence interaction can be described by the linear interaction approximation (LIA), provided that the shock wave width is much smaller than the turbulence scales and the upstream turbulent Mach number is modest [38]. Post-shock data of the shock-turbulence interaction at Taylor Reynolds number about 180 was generated by using LIA, and was used to study the effect of the plane shock wave on the vorticity dynamics and kinetic energy transfer of turbulence [40,41].

Shocklets can be generated from fluctuations of turbulent eddies in compressible turbulence at moderate and high turbulent Mach numbers. The term "eddy shocklets" was first introduced by Lee *et al.* [42] to describe the locally high compression structures in compressible turbulence, which exhibit characteristics of a typical shock wave, such as jumps of pressure, density, and temperature across the structures. There have been a number of interesting studies to address the statistics of shocklets [2,43,44], and the significant effects of shocklets on the statistical properties and spatial structures of compressible turbulence, including kinetic energy dissipation, vorticity production, intermittency, Lagrangian statistics, passive tracers and particles [43,45–52]. It is worth noting that the eddy shocklets were usually observed in decaying or solenoidally forced compressible isotropic turbulence at moderate to high turbulent Mach numbers ranging from 0.3 to 1.0. Recently, Wang *et al.* [44] studied the statistics of shocklets in the solenoidally forced compressible isotropic turbulence at turbulent Mach number ranging from 0.5 to 1.0. The PDFs of the shocklet strength and the jumps of the velocity and thermodynamic variables across the shocklet were found to exhibit a power-law scaling. Wang *et al.* [51] investigated the scaling and intermittency of the solenoidally forced compressible isotropic turbulence at turbulent Mach number ranging from 0.5 to 1.0. Statistical relations between the compressible velocity component and thermodynamic variables were studied by the shock jump conditions and numerical simulations. The relative scaling exponent of the structure functions of the compressible velocity component and thermodynamic variables was shown to saturate with an increase of the order. Wang *et al.* [53] applied the Favre filtering approach to study the kinetic energy transfer of the solenoidally forced compressible isotropic turbulence at turbulent Mach number ranging from 0.4 to 1.0. The subgrid-scale (SGS) kinetic energy flux was shown to be enhanced by shocklets. The net contribution of pressure dilatation to the average kinetic energy transfer was found to be negligibly small, due to the cancellation between compression and expansion work.

For the situation of stationary compressible isotropic turbulence driven by both solenoidal and compressible force components, large-scale shock waves can be generated, due to the significant fluctuations of compressible velocity component [21,54,55]. Wang *et al.* [21] investigated the interscale kinetic energy transfer of compressible isotropic turbulence in the presence of large-scale shock waves by using numerical simulations at turbulent Mach number $M_t = 0.62$. It was shown that the solenoidal component of kinetic energy spectrum exhibits a $k^{-5/3}$ scaling, while the compressible component of the kinetic energy spectrum exhibits a k^{-2} scaling. It was observed that both solenoidal and compressible components of SGS kinetic energy flux are nearly constant in an inertial range. Moreover, the SGS kinetic energy flux of the compressible mode was found to be larger than its solenoidal counterpart in the inertial range in their numerical simulations. Wang *et al.* [55] studied the statistics and structures of pressure and density of compressible isotropic turbulence in the presence of large-scale shock waves by using numerical simulations at turbulent Mach number $M_t = 0.73$. A -2 power-law scaling behavior was observed for the PDFs of the pressure gradient and pressure increment, and was explained by a statistical model. The average of density increment conditioned on the pressure increment was investigated by an heuristic model and numerical simulations. A positive correlation between the vorticity magnitude and pressure was identified, which was different from the situation of incompressible turbulence.

Recently, there are several interesting studies to address the compressibility effect on the energy transfer, coherent structure and intermittency in stationary compressible magnetohydrodynamic turbulence [56,57]. It was observed that the solenoidal velocity and the magnetic fields exhibit a $k^{-5/3}$ spectrum, while the compressible velocity exhibits a k^{-2} spectrum in compressible magnetohydrodynamic turbulence driven by both solenoidal and compressible force components [56]. Kinetic and magnetic energies were found to cascade conservatively from large to small scales. The conversion between kinetic and internal energy by pressure dilatation was shown to be dominated by the largest scale contributions. The saturated scaling exponents of high order structure functions of density and compressible velocity were identified, which could be attributed to the sheet-like current density structures and shocks [57].

There have been a number of studies on the statistics and scaling of supersonic turbulent flows, showing that the occurrence of shock waves causes distinct spectra and intermittency in supersonic turbulence [58–63]. Boldyrev *et al.* [58,59] extended the phenomenological model of She and Leveque [64] to supersonic turbulence, by assuming that the most dissipative structures are shock waves rather than vortex filaments. Kritsuk *et al.* [60] showed that the spectrum of

velocity $\mathbf{u}$ exhibited a $k^{-1.95}$ scaling and the spectrum of density-weighted velocity $\rho^{1/3}\mathbf{u}$ exhibited a $k^{-5/3}$ scaling in the inertial range, in a supersonic isothermal Euler turbulence at root mean square Mach number around 6. Schmidt *et al.* [61] pointed out that the scaling exponents for the structure functions of density-weighted velocity $\rho^{1/3}\mathbf{u}$ were universal for two different types of supersonic turbulence that are driven by solenoidal force and compressible force, respectively, at root-mean-square (rms) Mach number around 5.5. Konstandin *et al.* [62] observed that both Lagrangian and Eulerian structure functions exhibited higher intermittency in the supersonic turbulence driven by the compressible force as compare to those of the supersonic turbulence driven by the solenoidal force. Federrath [63] found that the spectrum of the density-weighted velocity $\rho^{1/3}\mathbf{u}$ exhibited a $k^{-1.74}$ scaling for the solenoidal force and exhibited a $k^{-2.10}$ scaling for the compressible force, in isothermal supersonic Euler turbulence at Mach number 17.

In this paper, we present a numerical study of statistics and scaling of stationary compressible isotropic turbulence driven by both solenoidal and compressible force components at grid resolution of 1024^3, and at turbulent Mach number M_t ranging from 0.30 to 0.65. We observe large-scale shock waves in our numerical simulations. We show that the statistical properties of the simulated flows are significantly different from those of solenoidally forced compressible isotropic turbulence [10,44,51]. In Sec. II, we present a brief description about the governing equations and numerical method. In Sec. III, we provide simulation parameters and one-point statistics of compressible turbulent flows. In Sec. IV, we investigate the spectra of velocity and thermodynamic variables. In Sec. V, we study the two-point statistics of simulated compressible turbulence. Moreover, we develop heuristic models for conditional average of increments of compressible velocity and thermodynamic variables based on the ideal shock relations. In Sec. VI, we present some discussions about the kinetic energy cascade of compressible turbulence, the different effects of shock waves and acoustic waves on the compressible velocity spectrum, and the physical insight on the models for conditional average based on the ideal shock relations. In Sec. VII, we provide a summary and conclusion of our study.

II. GOVERNING EQUATIONS AND NUMERICAL METHOD

We study compressible turbulence of ideal gas governed by the following dimensionless Navier-Stokes equations in conservation form [10]:

$$\frac{\partial \rho}{\partial t} + \frac{\partial(\rho u_j)}{\partial x_j} = 0, \tag{1}$$

$$\frac{\partial(\rho u_i)}{\partial t} + \frac{\partial[\rho u_i u_j + p\delta_{ij}]}{\partial x_j} = \frac{1}{\mathrm{Re}}\frac{\partial \sigma_{ij}}{\partial x_j} + \mathcal{F}_i, \tag{2}$$

$$\frac{\partial \mathcal{E}}{\partial t} + \frac{\partial[(\mathcal{E}+p)u_j]}{\partial x_j} = \frac{1}{\alpha}\frac{\partial}{\partial x_j}\left(\kappa\frac{\partial T}{\partial x_j}\right) + \frac{1}{\mathrm{Re}}\frac{\partial(\sigma_{ij}u_i)}{\partial x_j} - \Lambda + \mathcal{F}_j u_j, \tag{3}$$

$$p = \rho T/(\gamma M^2), \tag{4}$$

where ρ is the density, u_i is the velocity component, p is the pressure, and T is the temperature. $\mathcal{F}_i$ is a large-scale forcing to the fluid momentum, and Λ is a large-scale cooling function per unit volume. The viscous stress σ_{ij} is defined by

$$\sigma_{ij} = \mu\left(\frac{\partial u_i}{\partial x_j} + \frac{\partial u_j}{\partial x_i}\right) - \frac{2}{3}\mu\theta\delta_{ij}, \tag{5}$$

where, the velocity divergence θ is given by

$$\theta = \frac{\partial u_k}{\partial x_k}. \tag{6}$$

The total energy per unit volume $\mathcal{E}$ is defined by

$$\mathcal{E} = \frac{p}{\gamma - 1} + \frac{1}{2}\rho(u_j u_j). \tag{7}$$

In the governing equations of compressible turbulence, the hydrodynamic and thermodynamic variables are normalized by a set of reference scales, including the reference length L_f, velocity U_f, density ρ_f, pressure $p_f = \rho_f U_f^2$, temperature T_f, energy per unit volume $\rho_f U_f^2$, viscosity μ_f, and thermal conductivity κ_f [10]. After normalization, three reference governing parameters appear: the reference Reynolds number $\mathrm{Re} \equiv \rho_f U_f L_f/\mu_f$, the reference Mach number $M = U_f/c_f$, and the reference Prandtl number $\mathrm{Pr} \equiv \mu_f C_p/\kappa_f$. Here, the speed of sound is defined by $c_f \equiv \sqrt{\gamma R T_f}$. $\gamma \equiv C_p/C_v$ is the ratio of specific heat at constant pressure C_p to that at constant volume C_v, which is assumed to be equal to 1.4. R is the specific gas constant. The parameter α is defined by $\alpha = \mathrm{Pr}\,\mathrm{Re}(\gamma - 1)M^2$. It is assumed that the parameter Pr is equal to 0.7. The temperature-dependent viscosity μ and thermal conductivity κ are specified by the Sutherland's law [65]:

$$\mu = \frac{1.4042T^{1.5}}{T + 0.40417}, \tag{8}$$

$$\kappa = \frac{1.4042T^{1.5}}{T + 0.40417}. \tag{9}$$

Numerical simulations of compressible isotropic turbulence are performed in a cubic box of $(2\pi)^3$ with periodic boundary conditions. A hybrid compact-WENO scheme [65] is applied for the numerical simulations on a uniform grid with 1024^3 grid points. The hybrid scheme combines an eighth-order compact finite difference scheme [66] for smooth regions and a seventh-order WENO scheme [67] for shock regions. The velocity field is forced by fixing the energy spectrum within the two lowest wave-number shells. This force is applied to both solenoidal and compressible components of the velocity field [54,55,57,68,69]. The ratio of solenoidal to compressible energy component injected by this force is equal to 1. A spatially uniform thermal cooling Λ is applied to sustain the internal energy in a statistically steady state [65].

III. SIMULATION PARAMETERS AND ONE-POINT STATISTICS

The Taylor microscale Reynolds number Re_λ and the turbulent Mach number M_t of compressible turbulence are

TABLE I. Simulation parameters and resulting flow statistics.

Resolution	Re_λ	M_t	$\eta/\Delta x$	L_I/η	λ/η
1024^3	201	0.30	1.28	197	25.1
1024^3	196	0.40	1.30	193	24.5
1024^3	230	0.52	1.18	218	26.8
1024^3	234	0.65	1.04	244	27.3

TABLE III. Statistics of thermodynamic variables.

M_t	p_0	T_0	$p^{\rm rms}/p_0$	$\rho^{\rm rms}/\rho_0$	$T^{\rm rms}/T_0$
0.30	39.2	0.99	0.24	0.17	0.067
0.40	22.0	1.00	0.33	0.23	0.091
0.52	14.1	0.91	0.40	0.28	0.11
0.65	9.80	0.83	0.52	0.36	0.15

defined, respectively, by [6]

$$\mathrm{Re}_\lambda = \mathrm{Re}\frac{\langle\rho\rangle u'\lambda}{\sqrt{3}\langle\mu\rangle}, \tag{10}$$

and,

$$M_t = M\frac{u'}{\langle\sqrt{T}\rangle}, \tag{11}$$

where $\langle\rangle$ stands for ensemble average. The rms value of the velocity magnitude is given by $u' = \sqrt{\langle u_1^2+u_2^2+u_3^2\rangle}$ and the Taylor microscale is

$$\lambda = \sqrt{\frac{\langle u_1^2+u_2^2+u_3^2\rangle}{\langle(\partial u_1/\partial x_1)^2+(\partial u_2/\partial x_2)^2+(\partial u_3/\partial x_3)^2\rangle}}. \tag{12}$$

The Kolmogorov length scale η and the integral length scale L_I of compressible turbulence are defined, respectively, by [6]

$$\eta = [\langle\mu/(\mathrm{Re}\rho)\rangle^3/\epsilon]^{1/4}, \tag{13}$$

and

$$L_I = \frac{3\pi}{2(u')^2}\int_0^\infty \frac{E(k)}{k}dk, \tag{14}$$

where ϵ is the ensemble average of the dissipation rate of kinetic energy per unit mass:

$$\epsilon = \left\langle\frac{\sigma_{ij}S_{ij}}{Re\rho}\right\rangle. \tag{15}$$

$E(k)$ is the spectrum of kinetic energy per unit mass, namely, $\int_0^\infty E(k)dk = (u')^2/2$. The strain rate tensor S_{ij} is given by

$$S_{ij} = \frac{1}{2}\left(\frac{\partial u_i}{\partial x_j}+\frac{\partial u_j}{\partial x_i}\right). \tag{16}$$

Overall statistics of simulated compressible turbulence are summarized in Tables I–IV. The Taylor microscale Reynolds number is close to 200. There are four different turbulent Mach numbers: $M_t = 0.30$, 0.40, 0.52, and 0.65. The resolution parameter $\eta/\Delta x$ is in the range $1.04 \leqslant \eta/\Delta x \leqslant 1.30$, where Δx denotes the grid length in each direction. Consequently, the resolution parameter $k_{\max}\eta$ is in the range $3.27 \leqslant k_{\max}\eta \leqslant 4.08$, where the largest wave number, $k_{\max}$, is half of the number of grids N in each direction: $k_{\max} = N/2 = \pi/\Delta x$. The values of resolution parameters $\eta/\Delta x$ and $k_{\max}\eta$ in our simulations are similar to those in previous studies of stationary compressible isotropic turbulence [6,10,43,55].

By applying the Helmholtz decomposition, we decompose the velocity field $\mathbf{u}$ into a solenoidal component $\mathbf{u}^s$ and a compressible component $\mathbf{u}^c$ [1,2,6,9,10]:

$$\mathbf{u} = \mathbf{u}^s + \mathbf{u}^c, \tag{17}$$

where

$$\nabla\cdot\mathbf{u}^s = 0, \tag{18}$$

and,

$$\nabla\times\mathbf{u}^c = 0. \tag{19}$$

The rms values of the solenoidal and compressible velocity components are defined by $u^{s,\rm rms} = \sqrt{\langle(u_1^s)^2+(u_2^s)^2+(u_3^s)^2\rangle}$ and $u^{c,\rm rms} = \sqrt{\langle(u_1^c)^2+(u_2^c)^2+(u_3^c)^2\rangle}$, respectively. In Table II, we show that the ratio $u^{c,\rm rms}/u^{s,\rm rms}$ is in the range $0.64 \leqslant u^{c,\rm rms}/u^{s,\rm rms} \leqslant 0.69$, indicating that the magnitude of compressible velocity component is comparable to its solenoidal counterpart.

The rms values of velocity divergence and vorticity magnitude are defined by: $\theta' = \sqrt{\langle\theta^2\rangle}$ and $\omega' = \sqrt{\langle\omega_1^2+\omega_2^2+\omega_3^2\rangle}$, respectively. As shown in Table II, the ratio θ'/ω' is in the range $0.52 \leqslant \theta'/\omega' \leqslant 0.58$. The rms value of velocity divergence is nearly independent on the turbulent Mach number in our simulations, which is different from the situation of solenoidally forced compressible isotropic turbulence where θ' increases rapidly with the increase of M_t [9,44].

As shown in Table III, we calculate the rms values $p^{\rm rms}/p_0$, $\rho^{\rm rms}/\rho_0$, and $T^{\rm rms}/T_0$ of pressure, density and temperature normalized by their average values, respectively. Here, $p^{\rm rms} = \sqrt{\langle(p-p_0)^2\rangle}$, $\rho^{\rm rms} = \sqrt{\langle(\rho-\rho_0)^2\rangle}$, and $T^{\rm rms} = \sqrt{\langle(T-T_0)^2\rangle}$. The average values of thermodynamic variables are given by $p_0 = \langle p\rangle$, $\rho_0 = \langle\rho\rangle$, and $T_0 = \langle T\rangle$. The average density is $\rho_0 = 1$ in our numerical simulations. We observe that the normalized rms values of thermodynamic

TABLE II. Velocity statistics.

M_t	u'	$u^{c,\rm rms}$	$u^{s,\rm rms}$	$u^{c,\rm rms}/u^{s,\rm rms}$	θ'	ω'	θ'/ω'
0.30	2.19	1.24	1.81	0.69	9.1	17.6	0.52
0.40	2.21	1.24	1.82	0.68	9.7	17.4	0.56
0.52	2.23	1.20	1.88	0.64	10.1	17.5	0.58
0.65	2.19	1.24	1.81	0.69	11.2	19.5	0.57

TABLE IV. Normalized statistics of velocity and thermodynamic variables.

M_t	$\sqrt{\gamma\rho_0 p_0}u^{c,\rm rms}/p^{\rm rms}$	$\gamma p_0\rho^{\rm rms}/(\rho_0 p^{\rm rms})$	$\gamma p_0 T^{\rm rms}/[(\gamma-1)T_0 p^{\rm rms}]$
0.30	0.97	0.98	0.97
0.40	0.94	0.98	0.97
0.52	0.97	0.96	0.97
0.65	0.96	0.96	0.98

variables increase with the turbulent Mach number. Moreover, in Table IV, we present the following relations for different turbulent Mach numbers:

$$\frac{\sqrt{\gamma\rho_0 p_0}u^{c,\mathrm{rms}}}{p^{\mathrm{rms}}} \approx 1, \tag{20}$$

$$\frac{\gamma p_0 \rho^{\mathrm{rms}}}{\rho_0 p^{\mathrm{rms}}} \approx 1, \tag{21}$$

and

$$\frac{\gamma p_0 T^{\mathrm{rms}}}{(\gamma-1)T_0 p^{\mathrm{rms}}} \approx 1. \tag{22}$$

These observations are consistent with some previous studies of compressible isotropic turbulence [1,9,70].

We can derive the Eqs. (20)–(22) from ideal shock relationships in the situation of weak shocks. The jump of normal velocity across a shock can be written as [43,44]

$$\delta_s u_n = \sqrt{\frac{2(p_2-p_1)^2}{\rho_1[(\gamma+1)p_2+(\gamma-1)p_1]}}, \tag{23}$$

where $\delta_s u_n = |u_{2n} - u_{1n}|$. We name the variables upstream of the shock (lower density side) with subscript 1 and downstream of the shock (higher density side) with subscript 2. u_{1n} (or u_{2n}) is the velocity, projected along the shock normal direction, upstream (or downstream) of the shock relative to the shock front.

For the weak shocks, we assume that $\rho_1 \approx \rho_2 \approx \rho_0$, $p_1 \approx p_2 \approx p_0$, and $T_1 \approx T_2 \approx T_0$. We obtain the following approximation:

$$\delta_s u_n \approx \frac{u'}{\gamma M_t}\frac{\delta_s p}{p_0}, \tag{24}$$

where $\delta_s p = p_2 - p_1$. It is reasonable to make an approximation that the jump of the compressible velocity component is nearly equal to the jump of the normal velocity across a shock [44,51]. Then we have

$$\delta_s u^c \approx \frac{u'}{\gamma M_t}\frac{\delta_s p}{p_0}, \tag{25}$$

Therefore, the rms values $u^{c,\mathrm{rms}}$ and p^{rms} of fluctuations of compressible velocity and pressure induced by the ideal shock jump conditions satisfy

$$u^{c,\mathrm{rms}} \approx \frac{u'}{\gamma M_t}\frac{p^{\mathrm{rms}}}{p_0}. \tag{26}$$

Since $M_t \approx u'/\sqrt{\gamma p_0/\rho_0}$, we obtain Eq. (20).

From ideal shock relationship, the density ratio and the pressure ratio across a shock satisfy the following relation [2,43,44]:

$$\rho_r = \frac{(\gamma+1)p_r+\gamma-1}{(\gamma-1)p_r+\gamma+1}. \tag{27}$$

For a weak shock, we have the linear approximation:

$$\frac{\delta_s\rho}{\rho_0} \approx \frac{1}{\gamma}\frac{\delta_s p}{p_0}, \tag{28}$$

where $\delta_s\rho = \rho_2 - \rho_1$ and $\delta_s p = p_2 - p_1$. Thus, the rms values ρ^{rms} and p^{rms} of density and pressure induced by the ideal shock jump conditions satisfy

$$\frac{\rho^{\mathrm{rms}}}{\rho_0} \approx \frac{1}{\gamma}\frac{p^{\mathrm{rms}}}{p_0}. \tag{29}$$

The above equation is equivalent to Eq. (21). Equation (22) can be derived in a similar fashion.

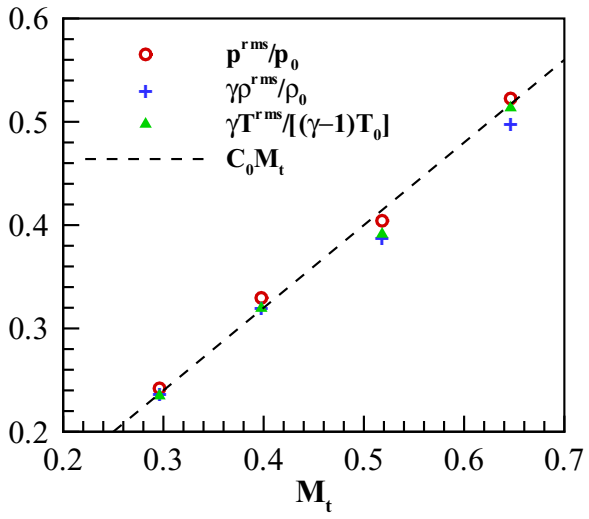

FIG. 1. Normalized rms values p^{rms}/p_0, $\gamma\rho^{\mathrm{rms}}/\rho_0$, and $\gamma T^{\mathrm{rms}}/[(\gamma-1)T_0]$ of pressure, density, and temperature, respectively, at turbulent Mach numbers $M_t = 0.30, 0.40, 0.52, 0.65$. Here, $C_0 = 0.8$.

In Fig. 1, we plot normalized rms values p^{rms}/p_0, $\gamma\rho^{\mathrm{rms}}/\rho_0$, and $\gamma T^{\mathrm{rms}}/[(\gamma-1)T_0]$ of pressure, density, and temperature, respectively, at turbulent Mach numbers $M_t = 0.30, 0.40, 0.52, 0.65$. We find that

$$\frac{p^{\mathrm{rms}}}{p_0} \approx \frac{\gamma\rho^{\mathrm{rms}}}{\rho_0} \approx \frac{\gamma T^{\mathrm{rms}}}{(\gamma-1)T_0} \approx C_0 M_t. \tag{30}$$

From Eq. (26), we show that

$$C_0 \approx \frac{\gamma u^{c,\mathrm{rms}}}{u'} \approx 0.8. \tag{31}$$

The theoretical relations Eqs. (30) and (31) are in good agreement with numerical results as shown in Fig. 1.

IV. SPECTRA OF VELOCITY AND THERMODYNAMIC VARIABLES

In Fig. 2, we plot the compensated spectrum $E(k)\epsilon^{-2/3}k^{5/3}$ of velocity field at different turbulent Mach numbers $M_t = 0.30, 0.40, 0.52, 0.65$, where $\int_0^\infty E(k)dk = \langle \mathbf{u}^2\rangle/2$. We can identify an inertial range of velocity spectrum, namely,

$$E(k)\epsilon^{-2/3}k^{5/3} \approx C_K, \tag{32}$$

where the Kolmogorov constant C_K is about 1.8, which is close to the values (1.5 to 2.0) typically observed for incompressible turbulent flows [71–73].

In Fig. 3, we show the compensated spectra $E^s(k)\epsilon^{-2/3}k^{5/3}$ and $E^c(k)\epsilon^{-2/3}k^{5/3}$ of the solenoidal and compressible components of velocity field at different turbulent Mach numbers $M_t = 0.30, 0.40, 0.52, 0.65$, where $\int_0^\infty E^s(k)dk = \langle(\mathbf{u}^s)^2\rangle/2$

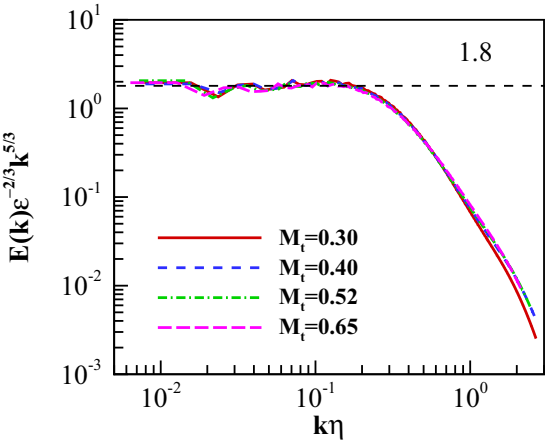

FIG. 2. Compensated spectrum $E(k)\epsilon^{-2/3}k^{5/3}$ of velocity field at different turbulent Mach numbers $M_t = 0.30, 0.40, 0.52, 0.65$.

and $\int_0^\infty E^c(k)dk = \langle(\mathbf{u}^c)^2\rangle/2$. We find the following relation:

$$E^s(k)\epsilon^{-2/3}k^{5/3} \approx 1.4, \tag{33}$$

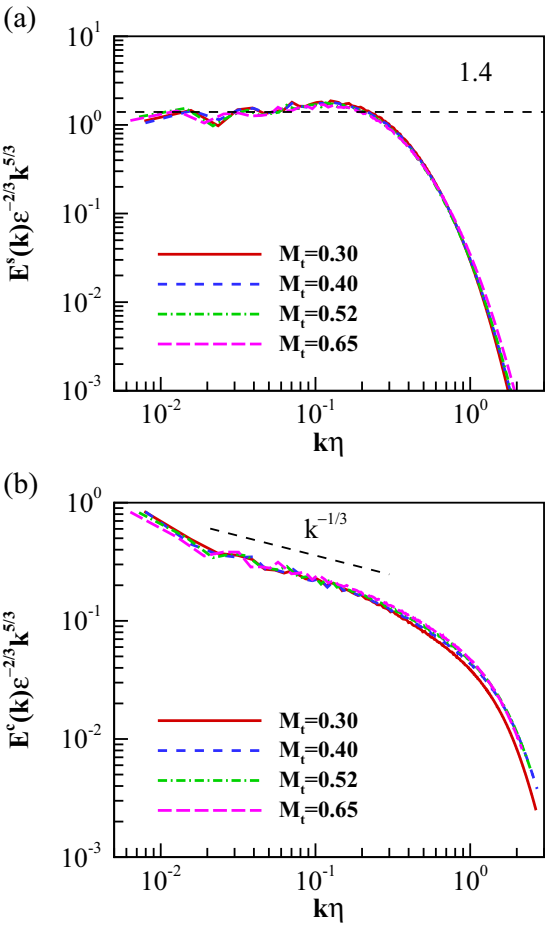

FIG. 3. Compensated spectra $E^s(k)\epsilon^{-2/3}k^{5/3}$ and $E^c(k)\epsilon^{-2/3}k^{5/3}$ of the solenoidal and compressible components of velocity field at different turbulent Mach numbers $M_t = 0.30, 0.40, 0.52, 0.65$.

which indicates that $E^s(k)$ exhibits a $k^{-5/3}$ scaling. We also show

$$E^c(k)\epsilon^{-2/3}k^{5/3} \sim k^{-1/3}, \tag{34}$$

which indicates that $E^c(k)$ exhibits a k^{-2} scaling. These observations are consistent with previous studies on numerical simulations of compressible isotropic turbulence driven by both solenoidal and compressible force components at $M_t = 0.62$ and $M_t = 0.73$ [21,55]. According to a previous study [21], large-scale shock waves can be generated by the compressible force component, giving rise to the k^{-2} spectrum of the compressible velocity component, which is similar to the Burgers turbulence [32]. Here, we confirm the k^{-2} spectrum of the compressible velocity component for turbulent Mach number ranging from 0.30 to 0.65. It is worth noting that the effect of Mach number on the spectrum of the compressible velocity component is negligibly small, which is different from the situation of solenoidally forced compressible isotropic turbulence where the spectrum of the compressible velocity component is highly dependent on the turbulent Mach number [10].

We depict contours of the normalized velocity divergence θ/θ' on arbitrarily selected x-y slices at turbulent Mach numbers $M_t = 0.30, 0.40, 0.52, 0.65$, in Fig. 4. We show that the features of expansion motions are very different from those of compression motions. High expansion regions $\theta/\theta' > 1$ are bloblike and spatially localized. High compression regions $\theta/\theta' < -1$ are much narrower and longer. The bandlike structures of high compression regions are shock waves [51,55,65]. Most strong expansion regions are close to some regions of strong compression. This observation is consistent with the physical insight that expansion regions can be identified just downstream of shock waves in compressible turbulence [43]. The spatial distributions of the normalized velocity divergence θ/θ' are similar to each other for different turbulent Mach numbers in our simulations. It is worth noting that in the situation of solenoidally forced compressible isotropic turbulence, the bandlike structures of high compression regions are obvious only for high turbulent Mach numbers $M_t \geqslant 0.8$ [51]. Thus, a finite ratio $(1:1)$ of compressible to solenoidal kinetic injection by large-scale external force can induce shock waves at much lower turbulent Mach numbers as compared with solenoidally forced compressible isotropic turbulence [44].

We present contours of the normalized density ρ/ρ_0 on the same slices as in Fig. 4, at turbulent Mach numbers $M_t = 0.30, 0.40, 0.52, 0.65$, in Fig. 5. Several severe discontinuities of the contours associated with strong compression can be identified, which represent the density jumps across shock waves. This observation is consistent with a previous study on the density and pressure of the compressible isotropic turbulence driven by both solenoidal and compressible force components at $M_t = 0.73$ [55]. Here, we observe similar spatial structures of shock waves for turbulent Mach number ranging from 0.30 to 0.65. In Fig. 6, we show contours of the normalized pressure p/p_0 and normalized temperature T/T_0 on the same slice as in Figs. 4 and 5, at turbulent Mach number $M_t = 0.65$. The contours of pressure and temperature exhibit frontlike structures in strong compression regions, which are very similar to those of density. Moreover, we observe that

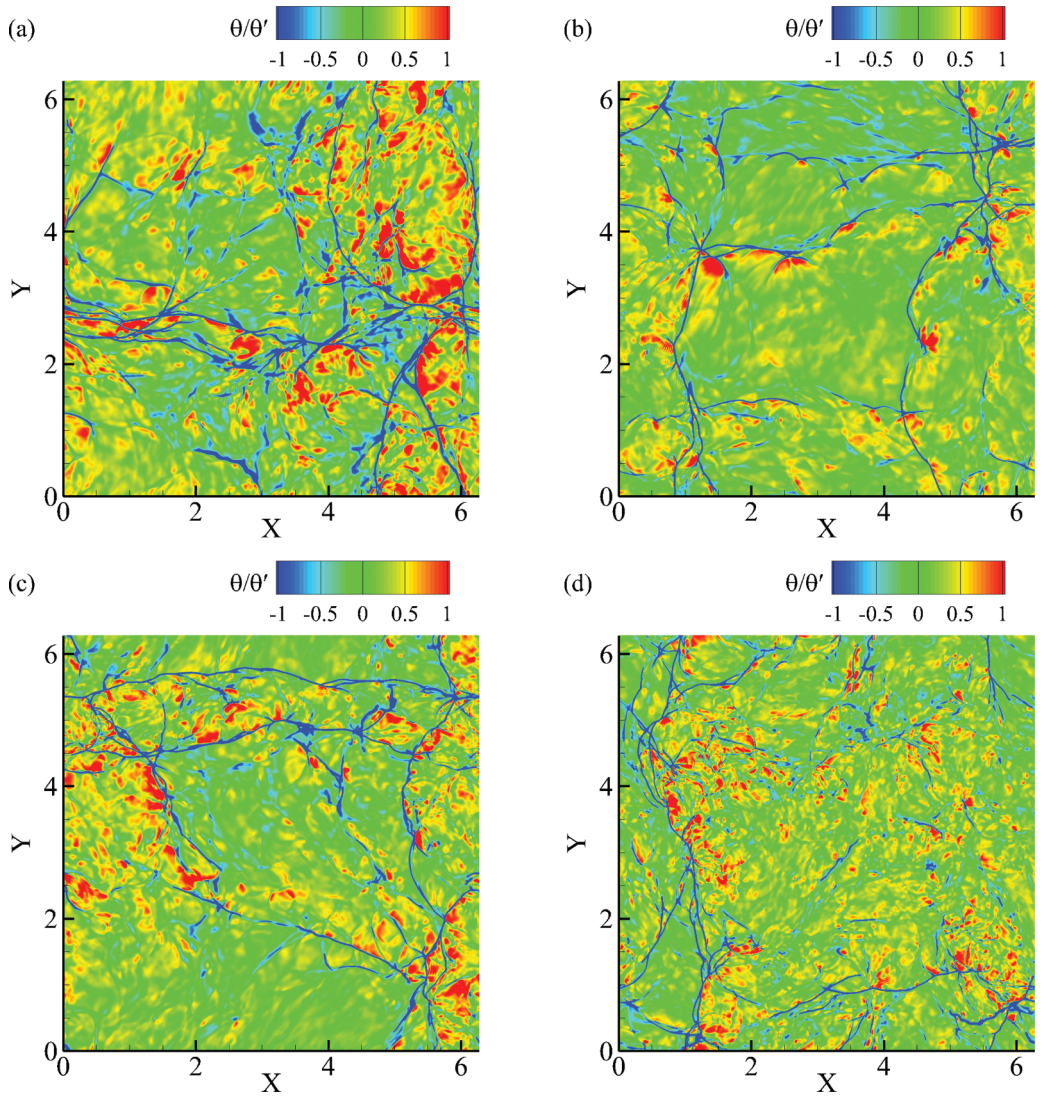

FIG. 4. Contours of the normalized velocity divergence θ/θ' on arbitrarily selected x-y slices, at turbulent Mach numbers (a) $M_t = 0.30$, (b) $M_t = 0.40$, (c) $M_t = 0.52$, (d) $M_t = 0.65$.

the fluctuations of normalized pressure p/p_0 are stronger than those of normalized temperature T/T_0 and normalized density ρ/ρ_0.

In Fig. 7, we plot the normalized spectra $E_N^\rho(k)$, $E_N^p(k)$, and $E_N^T(k)$ of density, pressure, and temperature, respectively, at different turbulent Mach numbers $M_t = 0.30, 0.40, 0.52, 0.65$, where $E_N^\rho(k) = E^\rho(k)/(\rho^{\rm rms})^2$, $E_N^p(k) = E^p(k)/(p^{\rm rms})^2$, and $E_N^T(k) = E^T(k)/(T^{\rm rms})^2$. Here, the spectra of density, pressure, and temperature satisfy $\int_0^\infty E^\rho(k)dk = \langle(\rho-\rho_0)^2\rangle$, $\int_0^\infty E^p(k)dk = \langle(p-p_0)^2\rangle$, and $\int_0^\infty E^T(k)dk = \langle(T-T_0)^2\rangle$, respectively [10]. We find that spectra of density, pressure, and temperature exhibit a k^{-2} scaling for different turbulent Mach numbers. The k^{-2} scaling of spectra of thermodynamic variables were already found in a previous study of the compressible isotropic turbulence driven by both solenoidal and compressible force components at $M_t = 0.73$ [55], which could be attributed to the occurrence of large-scale shock waves. It is worth noting that similar to the behaviors of spectra of velocity and its two components, the normalized spectra of thermodynamic variables are almost overlap one another at different turbulent Mach numbers in our simulations.

In the nearly isentropic weakly compressible turbulent flows, we have the following relations [10]:

$$\frac{(p-p_0)}{p_0} \approx \frac{\gamma(\rho-\rho_0)}{\rho_0} \approx \frac{\gamma(T-T_0)}{(\gamma-1)T_0}. \tag{35}$$

Generally, for any compressible flow, we can define the residual density and residual temperature as [10]

$$\rho^R = (\rho-\rho_0) - \frac{\rho_0(p-p_0)}{\gamma p_0}, \tag{36}$$

and

$$T^R = (T-T_0) - \frac{(\gamma-1)T_0(p-p_0)}{\gamma p_0}. \tag{37}$$

We consider the normalized spectra of the residual density and residual temperature: $E_R^\rho(k)/E^\rho(k)$ and $E_R^T(k)/E^T(k)$. Here, the spectra of the residual density and residual temperature satisfy $\int_0^\infty E_R^\rho(k)dk = \langle(\rho^R)^2\rangle$ and $\int_0^\infty E_R^T(k)dk = \langle(T^R)^2\rangle$.

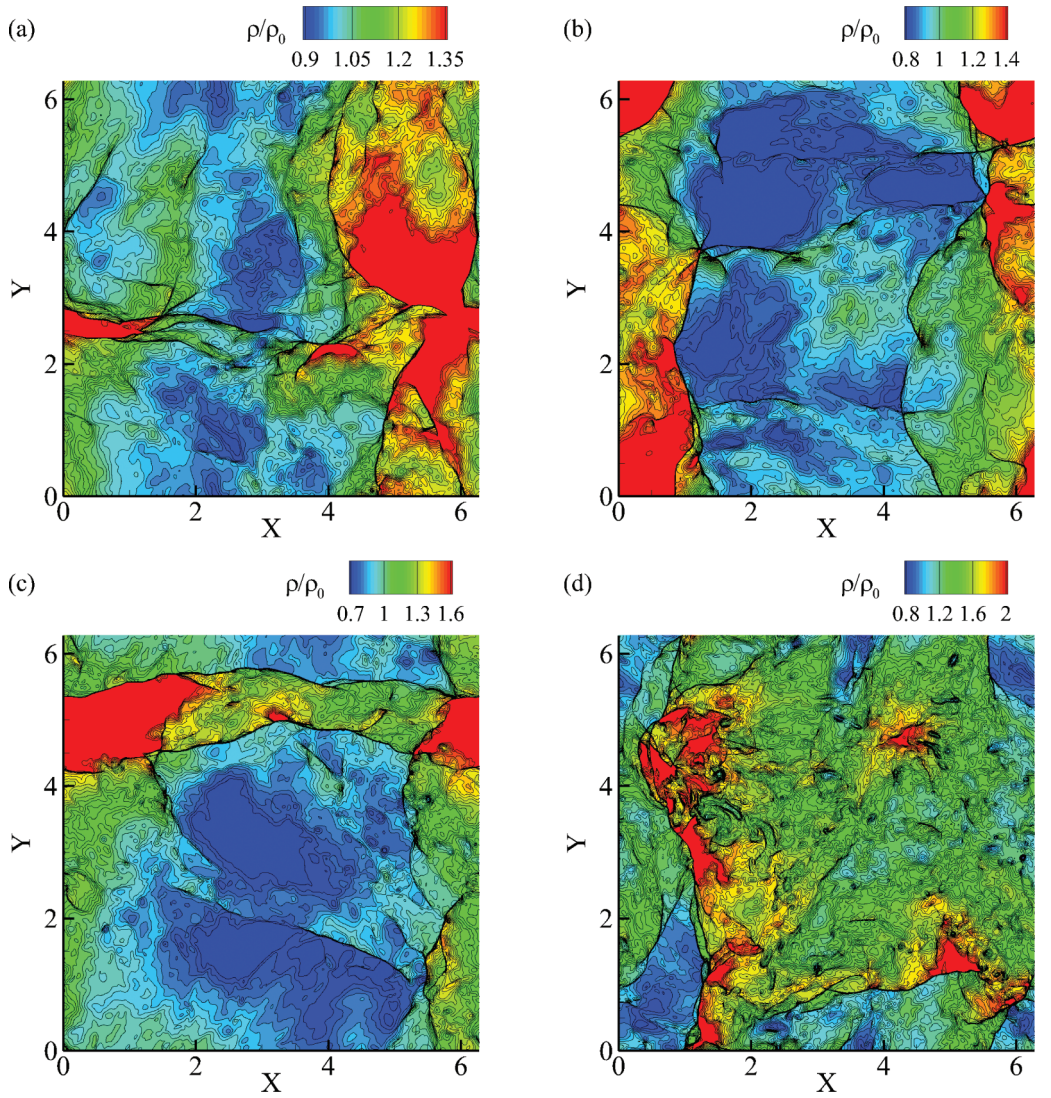

FIG. 5. Contours of the normalized density ρ/ρ_0 on the same slices as in Fig. 4, at turbulent Mach numbers (a) $M_t = 0.30$, (b) $M_t = 0.40$, (c) $M_t = 0.52$, (d) $M_t = 0.65$.

In Fig. 8, we plot the normalized spectra of the residual density and residual temperature at different turbulent Mach numbers $M_t = 0.30, 0.40, 0.52, 0.65$. We observe that the normalized spectra become larger as the turbulent Mach number increases. The normalized spectrum of the residual density is always much smaller than 1.0. Similarly, the normalized spectrum of the residual temperature is much smaller than 1.0 in the range $k\eta < 0.1$. These observations indicate that the spectra of density and temperature exhibit the same inertial scaling as the spectrum of pressure. The normalized spectrum of the residual temperature are close to 1.0 at small scales $k\eta \approx 1.0$, implying that the isentropic relations are no longer valid at small scales. We note that even though the exact isentropic relation is definitely violated at large-scale shock waves, the statistical isentropic relations of the spectra of pressure, density, and temperature can be identified at relatively large scales $k\eta < 0.1$, which may partially be attributed to the cancellation effect between low-entropy flows upstream of shock waves and high-entropy flows downstream of shock waves [55].

V. TWO-POINT STATISTICS OF COMPRESSIBLE TURBULENCE

We consider longitudinal structure functions of the compressible velocity component defined as [51]

$$S_n^{L,c}(r) \equiv \left\langle \left| \frac{\delta_r u^c}{u'} \right|^n \right\rangle, \tag{38}$$

where $\delta_r u^c = [\mathbf{u}^c(\mathbf{x}+\mathbf{r}) - \mathbf{u}^c(\mathbf{x})] \cdot \hat{\mathbf{r}}$ denotes the longitudinal increment of the compressible velocity component at the separation $\mathbf{r}$. Here, $\hat{\mathbf{r}} = \mathbf{r}/|\mathbf{r}|$. The structure functions are normalized by using the rms velocity u'. Similarly, we define structure functions of the density, pressure, and temperature by [51]

$$S_n^{\rho}(r) \equiv \left\langle \left| \frac{\delta_r \rho}{\rho_0} \right|^n \right\rangle, \tag{39}$$

$$S_n^{p}(r) \equiv \left\langle \left| \frac{\delta_r p}{p_0} \right|^n \right\rangle, \tag{40}$$

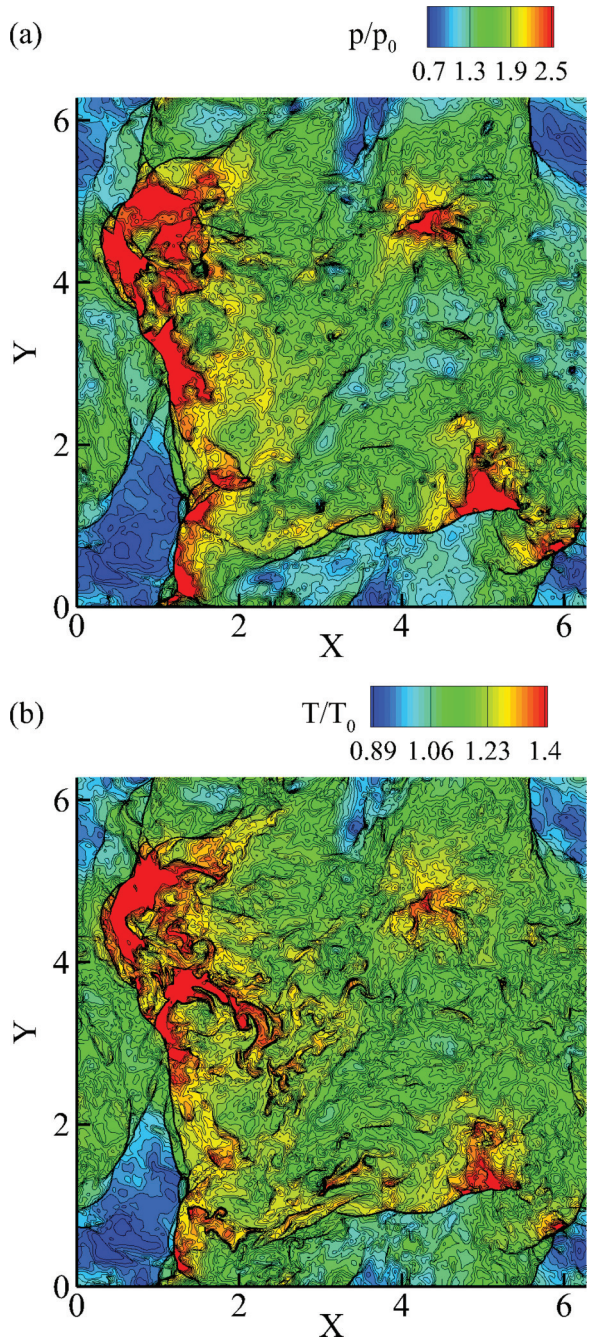

FIG. 6. Contours of the normalized pressure p/p_0 and normalized temperature T/T_0 on the same slice as in Figs. 4 and 5, at turbulent Mach number $M_t = 0.65$.

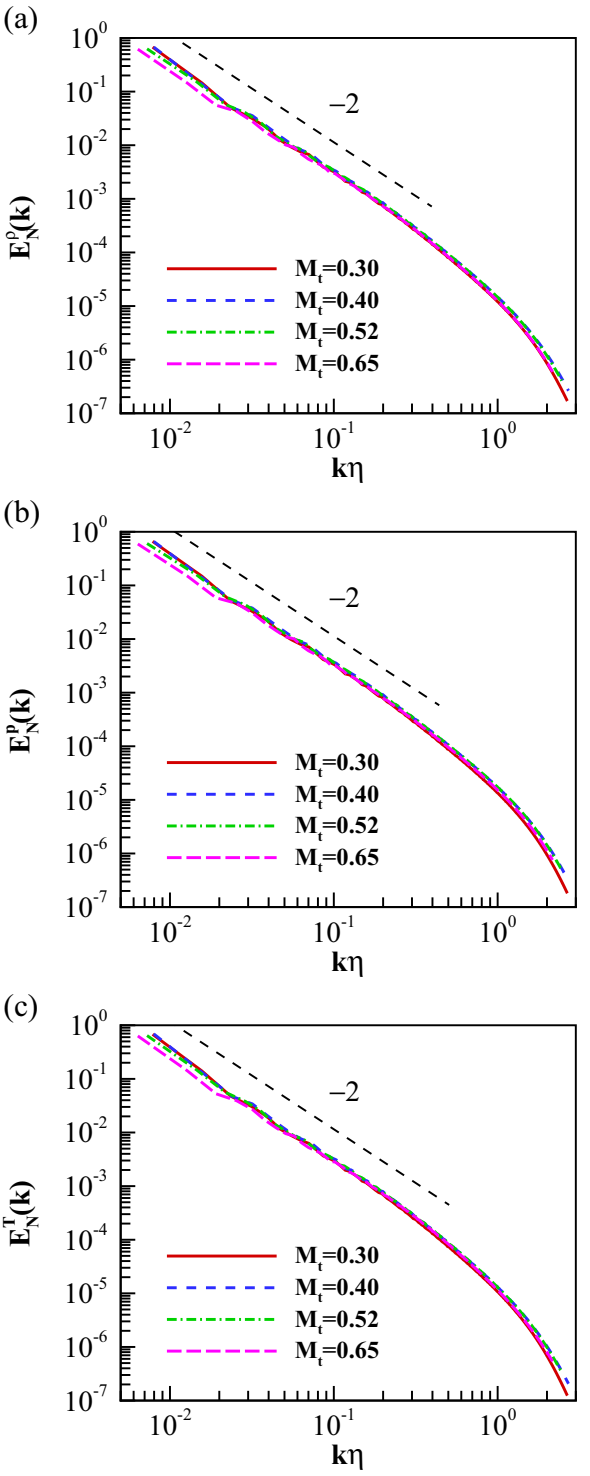

FIG. 7. Normalized spectra $E_N^\rho(k)$, $E_N^p(k)$, and $E_N^T(k)$ of density, pressure, and temperature at different turbulent Mach numbers $M_t = 0.30, 0.40, 0.52, 0.65$.

and

$$S_n^T(r) \equiv \left\langle \left| \frac{\delta_r T}{T_0} \right|^n \right\rangle, \tag{41}$$

where $\delta_r \rho = \rho(\mathbf{x}+\mathbf{r}) - \rho(\mathbf{x})$, $\delta_r p = p(\mathbf{x}+\mathbf{r}) - p(\mathbf{x})$, and $\delta_r T = T(\mathbf{x}+\mathbf{r}) - T(\mathbf{x})$ are, respectively, the increments of the density, pressure, and temperature at the separation $\mathbf{r}$. The structure functions are normalized by using the ensemble average values of the thermodynamic variables ρ_0, p_0, and T_0.

The structure functions can exhibit power-law scaling behaviors in the inertial range of turbulence. The power-law scaling exponents are denoted by $\zeta_n^{L,c}$, ζ_n^ρ, ζ_n^p, and ζ_n^T, for the compressible velocity component, density, pressure, and temperature, respectively [51],

$$S_n^{L,c}(r) \sim r^{\zeta_n^{L,c}}, \tag{42}$$

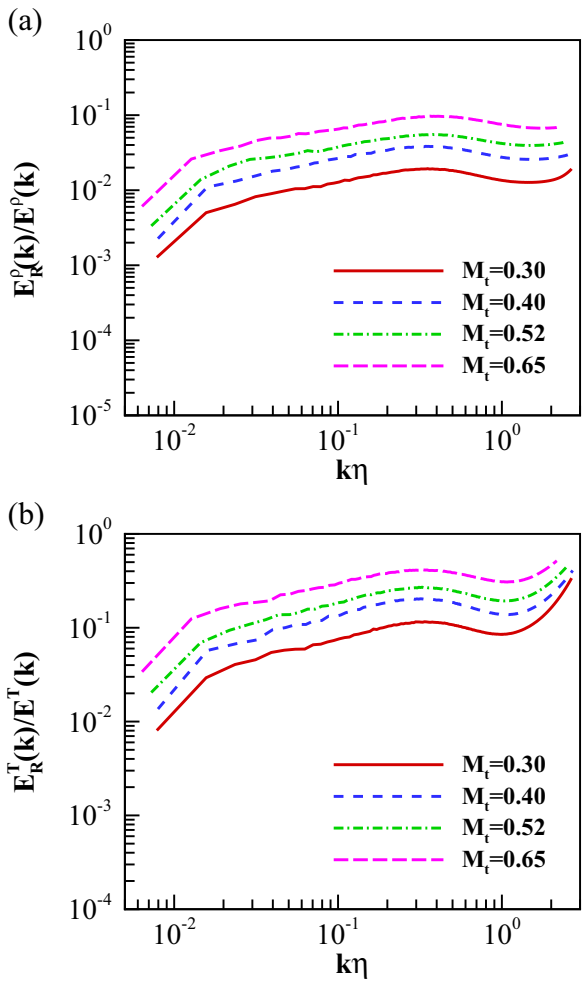

FIG. 8. Normalized spectra $E_R^\rho(k)/E^\rho(k)$ and $E_R^T(k)/E^T(k)$ of the residual density and residual temperature, respectively, at different turbulent Mach numbers $M_t = 0.30, 0.40, 0.52, 0.65$.

$$S_n^\rho(r) \sim r^{\zeta_n^\rho}, \tag{43}$$

$$S_n^p(r) \sim r^{\zeta_n^p}, \tag{44}$$

and

$$S_n^T(r) \sim r^{\zeta_n^T}. \tag{45}$$

In Figs. 9(a)–9(d), we present the structure functions $S_n^{L,c}(r)$, $S_n^\rho(r)$, $S_n^p(r)$, and $S_n^T(r)$ of the compressible velocity component and thermodynamic variables at orders from 1 to 6 for turbulent Mach number $M_t = 0.65$ in a log-log plot. We mark out the scale range $8 \leqslant r/\eta \leqslant 64$ by two dash lines, wherein the structure functions exhibit power-law scaling behaviors. The slopes of structure functions increase with the increase of order n. At high orders $n \geqslant 3$, the structure functions are parallel to one another, suggesting that the scaling exponents of structure functions can be saturated at $n \geqslant 3$. In Figs. 9(e) and 9(f), we depict the third-order structure functions $S_3^{L,c}(r)$ and $S_3^\rho(r)$ of the compressible velocity component and density at turbulent Mach numbers $M_t = 0.30, 0.40, 0.52, 0.65$. The third-order structure functions $S_3^{L,c}(r)$ of the compressible velocity component are nearly identical to each other for different turbulent Mach numbers. The third-order structure function of the density uniformly becomes larger at all scales as turbulent Mach number increases. However, the slope of the third-order structure function $S_3^\rho(r)$ is insensitive to the change of turbulent Mach number. We note that similar results can be obtained for the third-order structure functions of the pressure and temperature.

We calculate the scaling exponents $\zeta_n^{L,c}$, ζ_n^ρ, ζ_n^p, and ζ_n^T of structure functions of the compressible velocity component and thermodynamic variables at turbulent Mach numbers $M_t = 0.30, 0.40, 0.52, 0.65$, as shown in Fig. 10. The scaling exponent of the compressible velocity component becomes nearly constant at high orders $n \geqslant 3$ with the saturated value close to 1:

$$\zeta_\infty^{L,c} \approx 1. \tag{46}$$

This result signifies the similarity between the compressible velocity component of compressible isotropic turbulence and the velocity field in Burgers turbulence, both of which are dominated by large-scale shock waves. Similarly, the scaling exponents of density, pressure, and temperature are also saturated at high orders $n \geqslant 3$ with the saturated value close to 1:

$$\zeta_\infty^\rho \approx 1, \tag{47}$$

$$\zeta_\infty^p \approx 1, \tag{48}$$

and

$$\zeta_\infty^T \approx 1. \tag{49}$$

The scaling exponents of the compressible velocity component and thermodynamic variables are found to be nearly independent on the turbulent Mach number. In a previous study, it was revealed that the relative scaling exponents of the compressible velocity component and pressure saturate at high orders $n \geqslant 3$ in the solenoidally forced compressible isotropic turbulence at turbulent Mach number $M_t = 1.0$ [51].

We calculate the PDFs of the normalized increments of the compressible velocity component and thermodynamic variables: $P(\delta_r u^c/u^{c,\mathrm{rms}})$, $P(\delta_r \rho/\rho^{\mathrm{rms}})$, $P(\delta_r p/p^{\mathrm{rms}})$, and $P(\delta_r T/T^{\mathrm{rms}})$. In Fig. 11, we provide the normalized PDFs of the increments of the compressible velocity component and thermodynamic variables: $(r/\eta)^{-1}P(\delta_r u^c/u^{c,\mathrm{rms}})$, $(r/\eta)^{-1}P(\delta_r \rho/\rho^{\mathrm{rms}})$, $(r/\eta)^{-1}P(\delta_r p/p^{\mathrm{rms}})$, and $(r/\eta)^{-1}P(\delta_r T/T^{\mathrm{rms}})$ for the separations $r/\eta = 16, 24, 32, 48, 64$ at turbulent Mach number $M_t = 0.65$. We find that the left tails of the normalized PDFs $(r/\eta)^{-1}P(\delta_r u^c/u^{c,\mathrm{rms}})$ overlap one another for different separations. The right tail of the normalized PDFs $(r/\eta)^{-1}P(\delta_r u^c/u^{c,\mathrm{rms}})$ becomes longer with the increase of the separation r. Moreover, the left tail of the normalized PDFs $(r/\eta)^{-1}P(\delta_r u^c/u^{c,\mathrm{rms}})$ is much longer than the right tail. This observation indicates that the left tail has a major contribution to the high-order structure functions of the compressible velocity component. We show that the tails of the normalized PDFs of the increments of the density, pressure, and temperature nearly overlap one another for different separations. Moreover, the tails of the normalized PDFs of the pressure increments $(r/\eta)^{-1}P(\delta_r p/p^{\mathrm{rms}})$ are

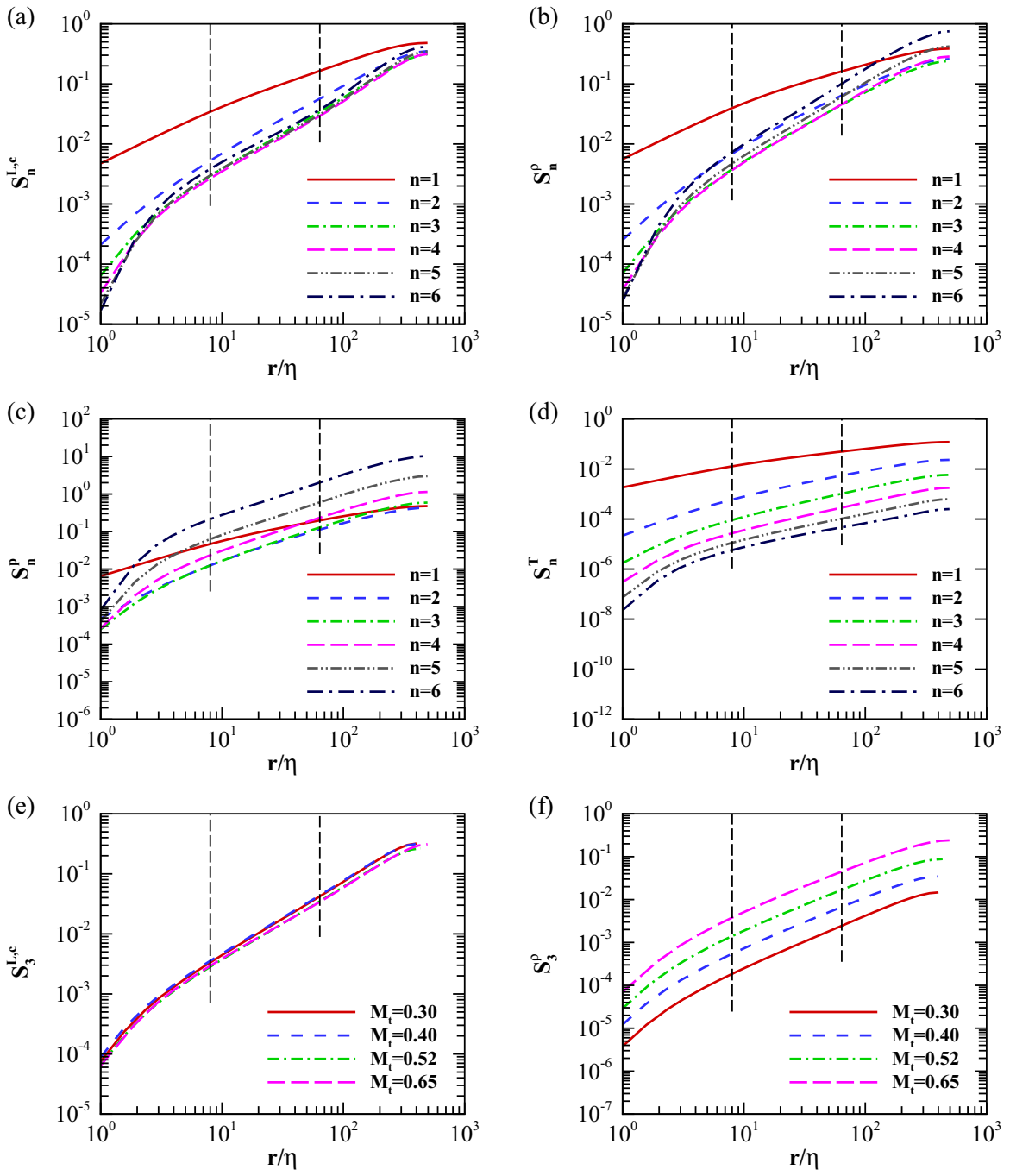

FIG. 9. Structure functions of the compressible velocity component and thermodynamic variables. The scale range $8 \leqslant r/\eta \leqslant 64$ is marked out by two dash lines. (a) $S_n^{L,c}(r)$ at $M_t = 0.65$; (b) $S_n^{\rho}(r)$ at $M_t = 0.65$; (c) $S_n^{p}(r)$ at $M_t = 0.65$; (d) $S_n^{T}(r)$ at $M_t = 0.65$; (e) $S_3^{L,c}(r)$ at $M_t = 0.30, 0.40, 0.52, 0.65$; (f) $S_3^{\rho}(r)$ at $M_t = 0.30, 0.40, 0.52, 0.65$.

longer than those of the normalized PDFs of the increments of the density and temperature $(r/\eta)^{-1}P(\delta_r\rho/\rho^{\rm rms})$ and $(r/\eta)^{-1}P(\delta_r T/T^{\rm rms})$. It is worth noting that the collapse of the tails of the PDFs of the increments of the compressible velocity component and thermodynamic variables by proper normalization indicates the saturation of the scaling exponents of structure functions [48,51,55,74,75], which is consistent with the previous observations in Fig. 10 that the scaling exponents of the compressible velocity component and thermodynamic variables are saturated at high orders $n \geqslant 3$ with the saturated value close to 1.

In Figs. 12(a)–12(d), we display the normalized PDFs of the increments of the compressible velocity component and thermodynamic variables: $(r/\eta)^{-1}P(-\delta_r u^c/u^{c,\rm rms})$, $(r/\eta)^{-1}P(\delta_r\rho/\rho^{\rm rms})$, $(r/\eta)^{-1}P(\delta_r p/p^{\rm rms})$, and $(r/\eta)^{-1}P(\delta_r T/T^{\rm rms})$ in a log-log plot, for the separations $r/\eta = 16, 24, 32, 48, 64$ at turbulent Mach number $M_t = 0.65$. The normalized PDFs exhibit a power-law region with the exponent close to -2. The -2 power-law region of the

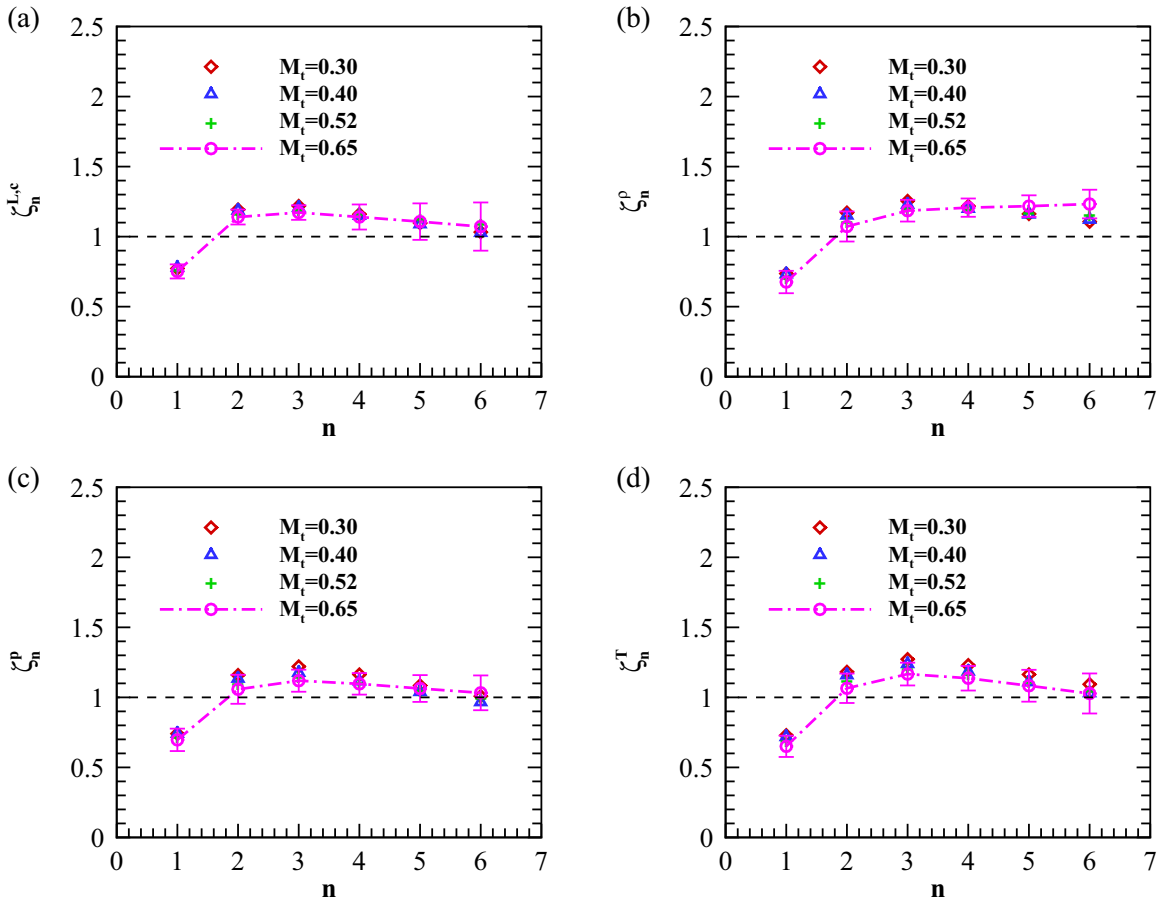

FIG. 10. Scaling exponents of structure functions of the compressible velocity component and thermodynamic variables at turbulent Mach numbers $M_t = 0.30, 0.40, 0.52, 0.65$. Errors include both statistical fluctuations and the uncertainty in the fit to the power-law scaling range. (a) $\zeta_n^{L,c}$; (b) ζ_n^{ρ}; (c) ζ_n^{p}; (d) ζ_n^{T}.

normalized PDFs can be also identified at other three turbulent Mach numbers $M_t = 0.30, 0.40, 0.52$, as shown in Figs. 12(e) and 12(f). In a previous study, the -2 power-law region of the normalized PDFs of the increments of pressure was identified in numerical simulations of the compressible isotropic turbulence driven by both solenoidal and compressible force components at $M_t = 0.73$ [55]. A heuristic PDF model was introduced to explain the power-law exponent -2. Here, we find the -2 power-law region of the normalized PDFs for the increments of the compressible velocity component and three thermodynamic variables at turbulent Mach numbers $M_t = 0.30, 0.40, 0.52, 0.65$.

We plot average of the increments of density and temperature conditioned on the pressure increment, for the separations $r/\eta = 16, 24, 32, 48, 64$ at turbulent Mach number $M_t = 0.65$ in Figs. 13(a) and 13(b). All the conditional average collapse to the same curve for the different separations, demonstrating the scale-invariant properties of the density, pressure and temperature. Due to the lack of samples in numerical simulations, the conditional average of the increments of density and temperature drop off rapidly for $|\delta_r p/p_0| > 5$. We begin to derive heuristic models of the conditional average of density and temperature based on ideal shock relations. From the Eq. (27) of the Rankine-Hugoniot jump condition of density ratio and pressure ratio across a shock, we obtain

$$\frac{\rho_2-\rho_1}{\rho_0} = \frac{1}{\gamma}\frac{\rho_1/\rho_0}{p_1/p_0}\frac{1}{1+\frac{(\gamma-1)p_0}{2\gamma p_1}\frac{p_2-p_1}{p_0}}\frac{p_2-p_1}{p_0}, \tag{50}$$

where, subscript 1 denotes the variables upstream of the shock and subscript 2 denotes the variables downstream of the shock. We make an approximation:

$$\frac{\rho_1/\rho_0}{p_1/p_0} \approx 1. \tag{51}$$

Equation (50) becomes

$$\frac{\rho_2-\rho_1}{\rho_0} \approx \frac{1}{\gamma\left[1+\frac{(\gamma-1)p_0}{2\gamma p_1}\frac{p_2-p_1}{p_0}\right]}\frac{p_2-p_1}{p_0}. \tag{52}$$

We introduce the following model for the increments of the density and pressure induced by the ideal shock jump condition:

$$\left\langle \frac{\delta_r\rho}{\rho_0} \middle| \frac{\delta_r p}{p_0} \right\rangle = \frac{1}{\gamma(1+C_1\delta_r p/p_0)}\frac{\delta_r p}{p_0}, \tag{53}$$

where, C_1 is a constant. In Fig. 13(a), we show that Eq. (53) is in good agreement with the numerical results for $C_1 = 4/35$, at $M_t = 0.65$. Similarly, we introduce the following model for the

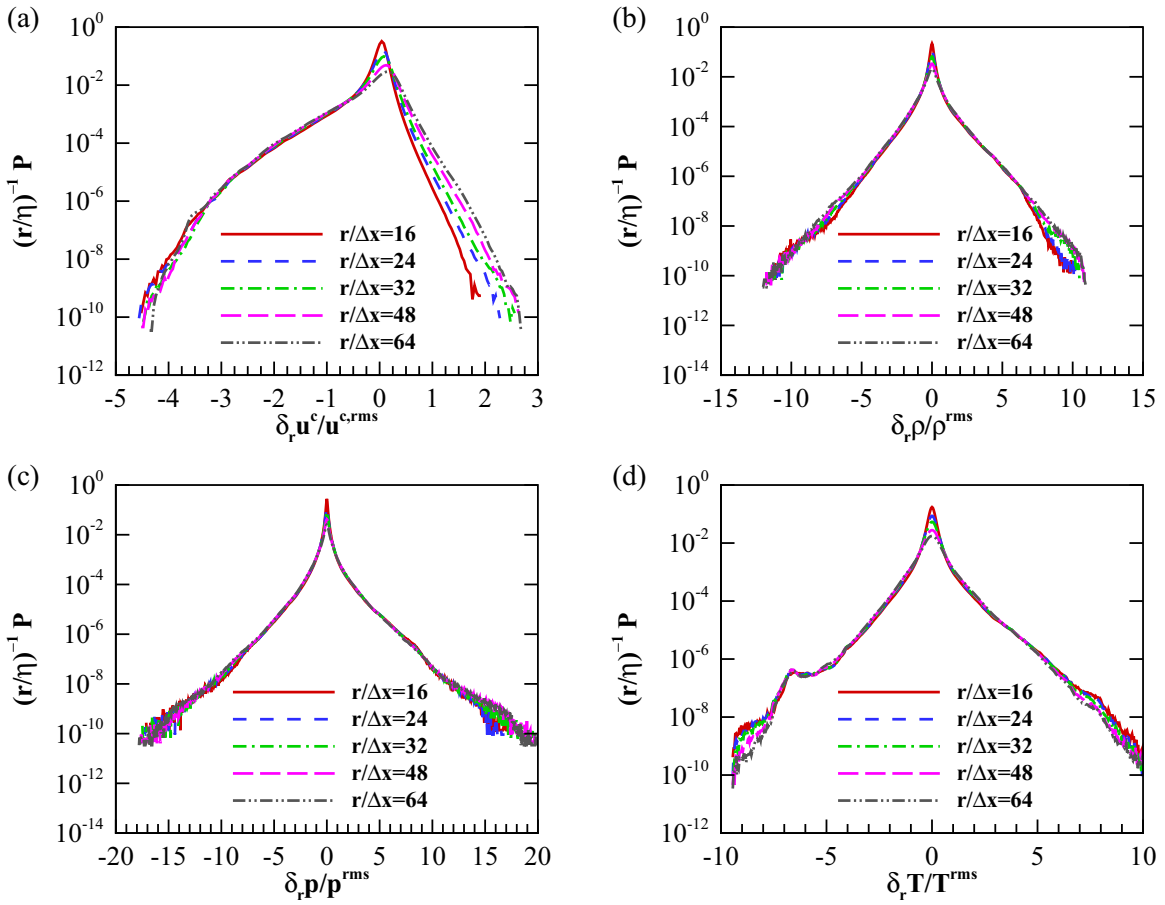

FIG. 11. Normalized PDFs of the increments of the compressible velocity component and thermodynamic variables for the separations $r/\eta = 16, 24, 32, 48, 64$ at turbulent Mach number $M_t = 0.65$. (a) $(r/\eta)^{-1} P(\delta_r u^c/u^{c,\mathrm{rms}})$; (b) $(r/\eta)^{-1} P(\delta_r \rho/\rho^{\mathrm{rms}})$; (c) $(r/\eta)^{-1} P(\delta_r p/p^{\mathrm{rms}})$; (d) $(r/\eta)^{-1} P(\delta_r T/T^{\mathrm{rms}})$.

average of temperature increment conditioned on the pressure increment:

$$\left\langle \frac{\delta_r T}{T_0} \middle| \frac{\delta_r p}{p_0} \right\rangle = \frac{\gamma - 1}{\gamma(1 + C_2 \delta_r p/p_0)} \frac{\delta_r p}{p_0}, \tag{54}$$

where C_2 is a constant. In Fig. 13(b), we find that Eq. (54) is in good agreement with the numerical results for $C_2 = 3/14$, at $M_t = 0.65$. From Eq. (53), we can derive a model for the average of the pressure increment conditioned on the density increment:

$$\left\langle \frac{\delta_r p}{p_0} \middle| \frac{\delta_r \rho}{\rho_0} \right\rangle = \frac{\gamma}{(1 - C_1 \gamma \delta_r \rho/\rho_0)} \frac{\delta_r \rho}{\rho_0}, \tag{55}$$

where $C_1 = 4/35$. Similarly, from Eqs. (53) and (54), we can derive a model for the average of the temperature increment conditioned on the density increment:

$$\left\langle \frac{\delta_r T}{T_0} \middle| \frac{\delta_r \rho}{\rho_0} \right\rangle = \frac{\gamma - 1}{(1 + C_3 \gamma \delta_r \rho/\rho_0)} \frac{\delta_r \rho}{\rho_0}, \tag{56}$$

where $C_3 = C_2 - C_1 = 1/10$. In Figs. 13(c) and 13(d), we observe that Eqs. (55) and (56) are consistent with the numerical results, at $M_t = 0.65$.

Moreover, we show that the conditional average of the increments of density and temperature collapse to the same curve for different turbulent Mach numbers $M_t = 0.30, 0.40, 0.52, 0.65$ in Figs. 13(e) and 13(f). Thus, model Eqs. (53) to (56) of the conditional average of the increments of thermodynamics are valid not only for different separations $r/\eta = 16, 24, 32, 48, 64$, but also for different turbulent Mach numbers $M_t = 0.30, 0.40, 0.52, 0.65$. In a previous study, a model for the conditional average $\langle \delta_r \rho/\rho^{\mathrm{rms}} | \delta_r p/p^{\mathrm{rms}} \rangle$ was proposed in the compressible isotropic turbulence driven by both solenoidal and compressible force components at $M_t = 0.73$ [55], where the rms values ρ^{rms} and p^{rms} were used to normalize the increments of the density and pressure. Here, we use the average values ρ_0, p_0, and T_0 to normalize the increments of the density, pressure and temperature. The behaviors of conditional average of increments of thermodynamic variables are quite universal for different turbulent Mach numbers in our numerical simulations.

We plot average of the increment of the compressible velocity component conditioned on the pressure increment, for the separations $r/\eta = 16, 24, 32, 48, 64$ at turbulent Mach numbers $M_t = 0.30, 0.40, 0.52, 0.65$. in Fig. 14. We observe that the conditional average $\langle \delta_r u^c/u' | \delta_r p/p_0 \rangle$ is always negative for $|\delta_r p|/p_0 > 0.5$. It is worth noting that the large magnitude of the increments of the compressible velocity component and thermodynamic variables can be

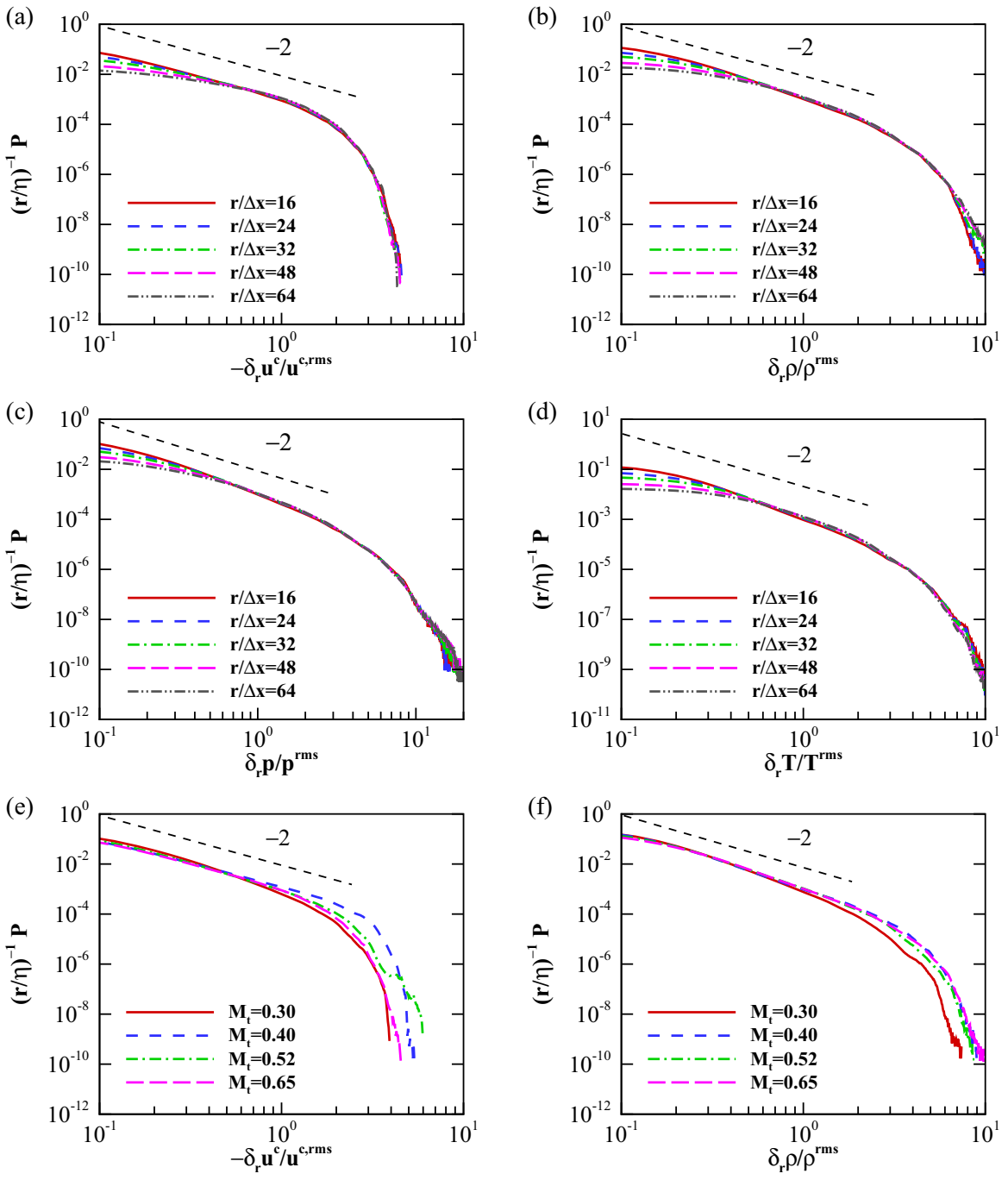

FIG. 12. Normalized PDFs of the increments of the compressible velocity component and thermodynamic variables in a log-log plot. (a) $(r/\eta)^{-1}P(-\delta_r u^c/u^{c,\mathrm{rms}})$ at $M_t = 0.65$; (b) $(r/\eta)^{-1}P(\delta_r \rho/\rho^{\mathrm{rms}})$ at $M_t = 0.65$; (c) $(r/\eta)^{-1}P(\delta_r p/p^{\mathrm{rms}})$ at $M_t = 0.65$; (d) $(r/\eta)^{-1}P(\delta_r T/T^{\mathrm{rms}})$ at $M_t = 0.65$; (e) $(r/\eta)^{-1}P(-\delta_r u^c/u^{c,\mathrm{rms}})$ for $r/\Delta x = 16$ at $M_t = 0.30, 0.40, 0.52, 0.65$; (f) $(r/\eta)^{-1}P(\delta_r \rho/\rho^{\mathrm{rms}})$ for $r/\Delta x = 16$ at $M_t = 0.30, 0.40, 0.52, 0.65$.

mainly attributed to the shock waves. The increment of the compressible velocity component tends to be negative across the shock wave, due to the strong compression of the shock wave. This observation is consistent with the fact that the left tail of the PDF of $\delta_r u^c/u^{c,\mathrm{rms}}$ is much longer than the right tail, demonstrating that the negative part of the increment of the compressible velocity component is more intermittent than its positive counterpart.

From Eq. (23) of the ideal shock condition, we have the following equation for the normal velocity jump $\delta_s u_n$:

$$\frac{\delta_s u_n}{u'} = \frac{1}{\gamma u'}\sqrt{\frac{\gamma p_1}{\rho_1}}\frac{1}{\sqrt{1+\frac{\gamma+1}{2\gamma}\frac{p_2-p_1}{p_1}}}\frac{p_2-p_1}{p_1}, \tag{57}$$

where subscript 1 denotes the variables upstream of the shock and subscript 2 denotes the variables downstream of the shock.

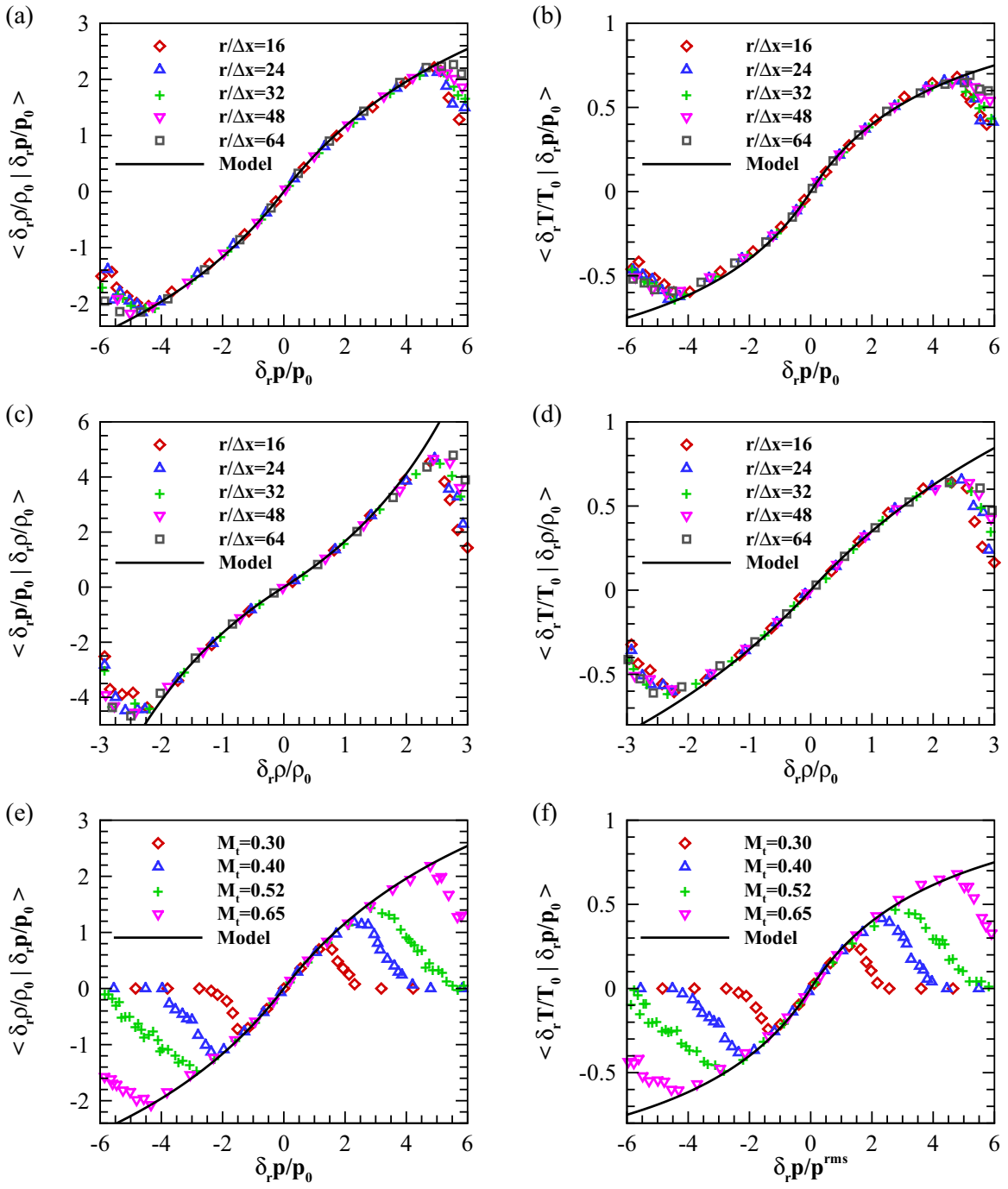

FIG. 13. Conditional average of the increments of density, pressure and temperature. (a) $\langle \delta_r \rho/\rho_0 | \delta_r p/p_0 \rangle$ at $M_t = 0.65$; (b) $\langle \delta_r T/T_0 | \delta_r p/p_0 \rangle$ at $M_t = 0.65$; (c) $\langle \delta_r p/p_0 | \delta_r \rho/\rho_0 \rangle$ at $M_t = 0.65$; (d) $\langle \delta_r T/T_0 | \delta_r \rho/\rho_0 \rangle$ at $M_t = 0.65$; (e) $\langle \delta_r \rho/\rho_0 | \delta_r p/p_0 \rangle$ for $r/\Delta x = 16$ at $M_t = 0.30, 0.40, 0.52, 0.65$; (f) $\langle \delta_r T/T_0 | \delta_r p/p_0 \rangle$ for $r/\Delta x = 16$ at $M_t = 0.30, 0.40, 0.52, 0.65$.

For the weak shocks, we assume that $p_1 \approx p_0$ and $\rho_1 \approx \rho_0$. Then, we obtain the following relation:

$$\frac{\delta_s u_n}{u'} \approx \frac{C_4}{\sqrt{1 + \frac{\gamma+1}{2\gamma}\frac{\delta_s p}{p_0}}} \frac{\delta_s p}{p_0}, \tag{58}$$

where $\delta_s p = p_2 - p_1$ denotes the pressure jump across the shock wave, and the coefficient $C_4 = 1/(\gamma M_t)$. Now, we introduce the following model for the conditional average of the increment of the compressible velocity component:

$$\left\langle \frac{\delta_r u^c}{u'} \middle| \frac{\delta_r p}{p_0} \right\rangle = -\frac{C_5}{\sqrt{1 + \frac{\gamma+1}{2\gamma}\frac{|\delta_r p|}{p_0}}} \frac{|\delta_r p|}{p_0}, \tag{59}$$

where the coefficient $C_5 = 0.42$. Equation (59) is roughly in agreement with the numerical results for relatively small $|\delta_r p|/p_0$. We note that the coefficient C_5 of the Eq. (59) does not depend on M_t in our numerical simulations, which is different from the Eq. (58), where the coefficient C_4 is

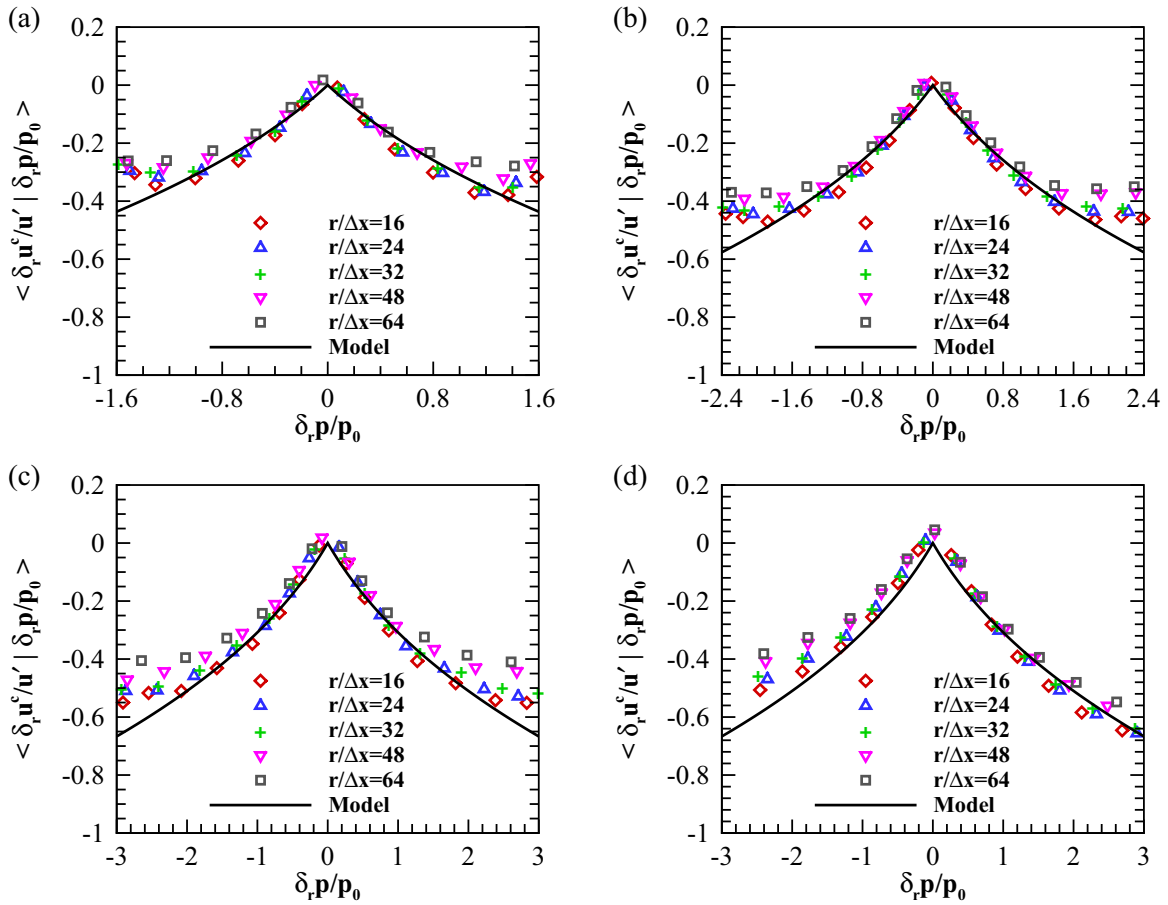

FIG. 14. Average of the increment of the compressible velocity component conditioned on the pressure increment, for the separations $r/\eta = 16$, 24, 32, 48, 64 at turbulent Mach numbers (a) $M_t = 0.30$, (b) $M_t = 0.40$, (c) $M_t = 0.52$, (d) $M_t = 0.65$.

proportional to M_t^{-1}. It is worth noting that the contribution of the negative component of $\delta_r u^c$ to the conditional average can be canceled partly by its positive component, giving rise to the fact that C_5 is smaller than C_4.

VI. DISCUSSION

According to previous studies on the numerical simulations of compressible turbulence, we infer that the solenoidal mode and compressible mode are only weakly coupled for turbulent Mach number $M_t \leqslant 1.0$ [7,21,53]. It was shown that in solenoidally forced compressible isotropic turbulence at turbulent Mach number about 1.0, the compressible mode occupies no more than 5% of total kinetic energy [7]. Moreover, the SGS kinetic energy flux of compressible mode was found to be no more than 10% of total SGS kinetic energy flux in solenoidally forced compressible isotropic turbulence at turbulent Mach numbers up to 1.0 [53]. These observations imply that the net kinetic energy transferred from solenoidal mode to compressible mode is quite small at $M_t \leqslant 1.0$.

It was shown by Wang *et al.* [21] that both solenoidal and compressible components of SGS kinetic energy flux are nearly constant in the inertial range in a stationary compressible isotropic turbulence driven by both solenoidal and compressible force components, implying that kinetic energies of both solenoidal and compressible modes cascade conservatively. The cascade of kinetic energy of solenoidal mode is similar to that in incompressible turbulence, giving rise to the Kolmogorov $k^{-5/3}$ scaling of solenoidal component of kinetic energy spectrum. The equation of the velocity potential Ψ defined by $\mathbf{u}^c = -\nabla\Psi$ was considered [21]:

$$\partial_t \Psi - \frac{1}{2}\nabla\Psi\cdot\nabla\Psi = \frac{4\nu}{3}\nabla^2\Psi + N_p + N_{\rm sol} + F, \qquad (60)$$

where, $N_p = \nabla^{-2}[\nabla\cdot(\nabla p/\rho)]$. $N_{\rm sol}$ denotes the effect of the solenoidal velocity component, which has small contribution to the equation of the velocity potential. F is the potential of external force. Similar to the theory of three-dimensional Burgers turbulence [32], the nonlinear effect of potential gradient square $\nabla\Psi\cdot\nabla\Psi$ gives rise to the generation of large-scale shock waves. Thus, the cascade of kinetic energy of compressible mode is similar to that in Burgers turbulence, leading to the k^{-2} scaling of compressible component of kinetic energy spectrum [21].

It is worth noting that the k^{-2} scaling of compressible velocity spectrum is attributed to the large-scale shock waves. If there is no large-scale shock wave in compressible turbulence, the compressible velocity spectrum can exhibit the scaling behavior with a different scaling exponent. In a previous study of solenoidally forced compressible isotropic turbulence by Wang *et al.* [10], it was shown that the spectrum of compressible velocity exhibit a k^{-3} scaling at small turbu-

lent Mach numbers $M_t \leqslant 0.1$ where the pseudosound mode dominates the compressible dynamics, while the spectrum of compressible velocity exhibit a $k^{-5/3}$ scaling at moderate turbulent Mach numbers $0.5 \leqslant M_t \leqslant 1.0$ where the acoustic mode dominates the compressible dynamics. It is worth noting that no cascade of kinetic energy of compressible mode is observed in the pseudosound-mode-dominated region, where the compressible velocity is fully enslaved to the solenoidal velocity [10]. Moreover, for compressible turbulence in the acoustic-mode-dominated region, the compressible dynamics can be approximated by linear wave equations [70]. Since there is no energy flux among different wave numbers in linear wave equations, the contribution of acoustic wave to the interscale kinetic energy transfer is probably weak.

Previous studies showed that the average of SGS kinetic energy flux is nearly constant in the inertial range of compressible turbulence, indicating that interscale kinetic energy transfer exhibits the scale-invariant property [21,53]. In this paper, we have demonstrated the scale-invariant property of the conditional average of increments of the compressible velocity component and thermodynamic variables by both heuristic models and numerical results. Moreover, the conditional average is shown to be insensitive to the change of turbulent Mach numbers for $0.30 \leqslant M_t \leqslant 0.65$ in our numerical simulations, where the interaction between the solenoidal and compressible modes is not significant.

Higher order statistics of the increments of the compressible velocity component and thermodynamic variables are necessary to demonstrate the intermittency of compressible mode and thermodynamic fields. The heuristic models of the conditional average of increments of the thermodynamic variables shown in Fig. 13 imply that the intermittency of temperature is weakest, while the intermittency of pressure is strongest. The observations are consistent with the normalized PDFs of increments of thermodynamic variables in Fig. 11: the tails of normalized PDF of temperature increment are shortest, while the tails of normalized PDF of pressure increment are longest.

VII. SUMMARY AND CONCLUSIONS

In this paper, we investigated the statistics and scaling of the velocity, density, pressure and temperature of the stationary compressible isotropic turbulence in the presence of large-scale shock waves at turbulent Mach number M_t ranging from 0.30 to 0.65. The turbulent flows are driven by both solenoidal and compressible force components. The ratio of the rms value of compressible velocity component to its solenoidal counterpart is kept nearly constant at different turbulent Mach numbers. It was found that the rms values of thermodynamic variables normalized by their mean values are in proportion to the turbulent Mach number. Some linear relations for the normalized rms values of the compressible velocity component and thermodynamic variables were derived from the ideal shock conditions, and were verified by numerical simulations.

The spectra for the velocity and its solenoidal component exhibit a $k^{-5/3}$ scaling, while the spectra for the compressible velocity component and thermodynamic variables exhibit a k^{-2} scaling. The normalized spectra of the compressible velocity component and thermodynamic variables were found to be nearly independent on the turbulent Mach number. The statistical isentropic relations of the spectra of pressure, density and temperature were identified at relatively large scales $k\eta < 0.1$.

The scaling exponents of the structure functions of the compressible velocity component and thermodynamic variables are saturated at high orders $n \geqslant 3$ with the saturated value close to 1.0, similar to Burgers turbulence. The tails of the normalized PDFs of increments of the compressible velocity component and thermodynamic variables overlap one another for different separations r, and exhibit a -2 power-law scaling at different turbulent Mach numbers. The conditional average of increments of the compressible velocity component and thermodynamic variables overlap one another for different separations r and different turbulent Mach numbers. Some models based on the ideal shock conditions were proposed for the conditional average, and were found to be consistent with the numerical simulations.

Finally, we have pointed out that the solenoidal and compressible modes are only weakly coupled for $0.30 \leqslant M_t \leqslant 0.65$ in our numerical simulations. The spectrum and kinetic energy transfer of compressible mode are closely related to the large-scale shock waves, which can be partly explained by the theory of three-dimensional Burgers turbulence. Moreover, the effect of shock wave on the statistics of compressible mode is different from that of acoustic wave, since shock wave is a strongly nonlinear phenomenon, while acoustic wave can be described approximately by linear wave equations. The statistical properties investigated in the present study are helpful for developing turbulence models of compressible turbulence in the presence of large-scale shock waves. Numerical simulations at higher turbulent Mach numbers are required to further investigate the interactions between the solenoidal and compressible modes.

ACKNOWLEDGMENTS

The authors appreciate the valuable comments of the anonymous referees. This work was supported by the National Natural Science Foundation of China (NSFC Grants No. 11702127, No. 91752201, and No. 11672123), by "the Thousand Talents Plan for Young Professionals," and by the Technology and Innovation Commission of Shenzhen Municipality (Grant No. JCYJ20170412151759222). J.W. acknowledges the support from Young Elite Scientist Sponsorship Program by CAST (Grant No. 2016QNRC001).

[1] P. Sagaut and C. Cambon, *Homogeneous Turbulence Dynamics* (Cambridge University Press, Cambridge, England, 2008).
[2] R. Samtaney, D. I. Pullin, and B. Kosovic, Phys. Fluids **13**, 1415 (2001).
[3] S. Pirozzoli and F. Grasso, Phys. Fluids **16**, 4386 (2004).
[4] M. R. Petersen and D. Livescu, Phys. Fluids **22**, 116101 (2010).
[5] S. Suman and S. S. Girimaji, J. Fluid Mech. **683**, 289 (2011).
[6] J. Wang, Y. Shi, L.-P. Wang, Z. Xiao, X. T. He, and S. Chen, J. Fluid Mech. **713**, 588 (2012).

[7] J. Wang, Y. Shi, L.-P. Wang, Z. Xiao, X. T. He, and S. Chen, Phys. Rev. Lett. **108**, 214505 (2012).
[8] D. Li, X. Zhang, and G. He, Phys. Rev. E **88**, 021001(R) (2013).
[9] S. Jagannathan and D. A. Donzis, J. Fluid Mech. **789**, 669 (2016).
[10] J. Wang, T. Gotoh, and T. Watanabe, Phys. Rev. Fluids **2**, 013403 (2017).
[11] L. Sciacovelli, P. Cinnella, and F. Grasso, J. Fluid Mech. **825**, 515 (2017).
[12] S. Pan and E. Johnsen, J. Fluid Mech. **833**, 717 (2017).
[13] U. Frisch, *Turbulence: The Legacy of A. N. Kolmogorov* (Cambridge University Press, Cambridge, England, 1995).
[14] H. Aluie, Phys. Rev. Lett. **106**, 174502 (2011).
[15] H. Aluie, Physica D **247**, 54 (2013).
[16] H. Aluie, S. Li, and H. Li, Astrophys. J. Lett. **751**, L29 (2012).
[17] G. Falkovich, I. Fouxon, and Y. Oz, J. Fluid Mech. **644**, 465 (2010).
[18] R. Wagner, G. Falkovich, A. G. Kritsuk, and M. L. Norman, J. Fluid Mech. **713**, 482 (2012).
[19] S. Galtier and S. Banerjee, Phys. Rev. Lett. **107**, 134501 (2011).
[20] A. G. Kritsuk, R. Wagner, and M. L. Norman, J. Fluid. Mech. **729**, R1 (2013).
[21] J. Wang, Y. Yang, Y. Shi, Z. Xiao, X. T. He, and S. Chen, Phys. Rev. Lett. **110**, 214505 (2013).
[22] G. L. Eyink and T. D. Drivas, Phys. Rev. X **8**, 011022 (2018).
[23] J. M. Burgers, *Advances in Applied Mechanics* (Academic, New York, 1948), Vol. I, pp. 171–199.
[24] E. Aurell, U. Frisch, J. Lutsko, and M. Vergassola, J. Fluid. Mech. **238**, 467 (1992).
[25] D. Mitra, J. Bec, R. Pandit, and U. Frisch, Phys. Rev. Lett. **94**, 194501 (2005).
[26] A. M. Polyakov, Phys. Rev. E **52**, 6183 (1995).
[27] V. Yakhot and A. Chekhlov, Phys. Rev. Lett. **77**, 3118 (1996).
[28] T. Gotoh and R. H. Kraichnan, Phys. Fluids **10**, 2859 (1998).
[29] Weinan E, K. Khanin, A. Mazel, and Ya. Sinai, Phys. Rev. Lett. **78**, 1904 (1997).
[30] J. Bec, Phys. Rev. Lett. **87**, 104501 (2001).
[31] S. Boldyrev, T. Linde, and A. Polyakov, Phys. Rev. Lett. **93**, 184503 (2004).
[32] J. Bec and K. Khanin, Phys. Rep. **447**, 1 (2007).
[33] J. Cardy, G. Falkovich, and K. Gawedzki, *Nonequilibrium Statistical Mechanics and Turbulence* (Cambridge University Press, Cambridge, England, 2008).
[34] S. Lee, S. K. Lele, and P. Moin, J. Fluid Mech. **251**, 533 (1993).
[35] Y. Andreopoulos, J. H. Agui, and G. Briassulis, Annu. Rev. Fluid Mech. **32**, 309 (2000).
[36] J. Larsson and S. K. Lele, Phys. Fluids **21**, 126101 (2009).
[37] J. Larsson, I. Bermejo-Moreno, and S. K. Lele, J. Fluid Mech. **717**, 293 (2013).
[38] J. Ryu and D. Livescu, J. Fluid Mech. **756**, R1 (2014).
[39] R. Quadros, K. Sinha, and J. Larsson, J. Fluid Mech. **796**, 113 (2016).
[40] D. Livescu and J. Ryu, Shock Waves **26**, 241 (2016).
[41] D. Livescu and Z. Li, AIP Conf. Proc. **1793**, 150009 (2017).
[42] S. Lee, S. Lele, and P. Moin, Phys. Fluids A **3**, 657 (1991).
[43] J. Wang, Y. Shi, L.-P. Wang, Z. Xiao, X. T. He, and S. Chen, Phys. Fluids **23**, 125103 (2011).
[44] J. Wang, T. Gotoh, and T. Watanabe, Phys. Rev. Fluids **2**, 023401 (2017).
[45] S. Kida and S. A. Orszag, J. Sci. Comput. **5**, 1 (1990).
[46] Y. Yang, J. Wang, Y. Shi, Z. Xiao, X. T. He, and S. Chen, Phys. Rev. Lett. **110**, 064503 (2013).
[47] Y. Yang, J. Wang, Y. Shi, Z. Xiao, X. T. He, and S. Chen, Phys. Fluids **26**, 091702 (2014).
[48] Y. Yang, J. Wang, Y. Shi, Z. Xiao, X. T. He, and S. Chen, J. Fluid Mech. **786**, R6 (2016).
[49] Z. Xia, Y. Shi, Q. Zhang, and S. Chen, Phys. Fluids **28**, 016103 (2016).
[50] Q. Zhang, H. Liu, Z. Ma, and Z. Xiao, Phys. Fluids **28**, 055104 (2016).
[51] J. Wang, T. Gotoh, and T. Watanabe, Phys. Rev. Fluids **2**, 053401 (2017).
[52] Q. Dai, K. Luo, T. Jin, and J. Fan, J. Fluid Mech. **832**, 438 (2017).
[53] J. Wang, M. Wan, S. Chen, and S. Y. Chen, J. Fluid Mech. **841**, 581 (2018).
[54] S. Kida and S. A. Orszag, J. Sci. Comput. **5**, 85 (1990).
[55] J. Wang, Y. Yang, Y. Shi, Z. Xiao, X. He, and S. Chen, J. Turblence **14**, 21 (2013).
[56] Y. Yang, Y. Shi, M. Wan, W. H. Matthaeus, and S. Chen, Phys. Rev. E **93**, 061102 (2016).
[57] Y. Yang, W. H. Matthaeus, Y. Shi, M. Wan, and S. Chen, Phys. Fluids **29**, 035105 (2017).
[58] S. Boldyrev, A. Nordlund, and P. Padoan, Astrophys. J. **573**, 678 (2002).
[59] S. Boldyrev, A. Nordlund, and P. Padoan, Phys. Rev. Lett. **89**, 031102 (2002).
[60] A. Kritsuk, M. Norman, P. Padoan, and R. Wagner, Astrophys. J. **665**, 416 (2007).
[61] W. Schmidt, C. Federrath, and R. Klessen, Phys. Rev. Lett. **101**, 194505 (2008).
[62] L. Konstandin, C. Federrath, R. Klessen, and W. Schmidt, J. Fluid Mech. **692**, 183 (2012).
[63] C. Federrath, Mon. Not. R. Astron. Soc. **436**, 1245 (2013).
[64] Z. S. She and E. Leveque, Phys. Rev. Lett. **72**, 336 (1994).
[65] J. Wang, L.-P. Wang, Z. Xiao, Y. Shi, and S. Chen, J. Comp. Phys. **229**, 5257 (2010).
[66] S. K. Lele, J. Comput. Phys. **103**, 16 (1992).
[67] D. S. Balsara and C. W. Shu, J. Comput. Phys. **160**, 405 (2000).
[68] H. Miura and S. Kida, Phys. Fluids **7**, 1732 (1995).
[69] C. Federrath, J. Roman-Duval, R. S. Klessen, W. Schmidt, and M. Mac Low, Astron. Astrophys. **512**, A81 (2010).
[70] S. Sarkar, G. Erlebacher, M. Y. Hussaini, and H. O. Kreiss, J. Fluid Mech. **227**, 473 (1991).
[71] L.-P. Wang, S. Chen, J. G. Brasseur, and J. C. Wyngaard, J. Fluid Mech. **309**, 113 (1996).
[72] T. Watanabe and T. Gotoh, New J. Phys. **6**, 40 (2004).
[73] T. Watanabe and T. Gotoh, J. Fluid Mech. **590**, 117 (2007).
[74] T. Watanabe and T. Gotoh, Phys. Fluids **18**, 058105 (2006).
[75] R. Benzi, L. Biferale, R. T. Fisher, L. P. Kadanoff, D. Q. Lamb, and F. Toschi, Phys. Rev. Lett. **100**, 234503 (2008).